

PARAMETRIC LEVEL-SETS ENHANCED TO IMPROVE RECONSTRUCTION (PALENTIR)

EGE OZSAR, MISHA KILMER, ERIC MILLER, ERIC DE STURLER, ARVIND SAIBABA

Abstract. For inverse problems where one is concerned with recovering the shape and contrast of an unknown number of objects embedded in a medium, parametric level set (PaLS) methods provide much of the flexibility of traditional level set methods while avoiding many of the difficulties such as regularization, re-initialization. In this paper, we consider the restoration and reconstruction of piecewise constant objects in two and three dimensions using PaLEnTIR, a significantly enhanced PaLS model relative to the current state-of-the-art. The primary contribution of this paper is a new PaLS formulation which requires only a single level set function to recover a scene with piecewise constant objects possessing multiple unknown contrasts. Our model offers distinct advantages over current approaches to the multi-contrast, multi-object problem, all of which require multiple level sets and explicit estimation of the contrast magnitudes. Given upper and lower bounds on the contrast, our approach is able to recover objects with any distribution of contrasts and eliminates the need to know either the number of contrasts in a given scene or their values. We provide an iterative process for finding these space-varying contrast limits. Relative to most PaLS methods which employ radial basis functions (RBFs), our model makes use of non-isotropic basis functions, thereby expanding the class of shapes that a PaLS model of a given complexity can approximate. Finally, PaLEnTIR improves the conditioning of the Jacobian matrix required as part of the parameter identification process and consequently accelerates the optimization methods by controlling the magnitude of the PaLS expansion coefficients, fixing the centers of the basis functions, and the uniqueness of parametric to image mappings provided by the new parameterization. We demonstrate the performance of the new approach using both 2D and 3D variants of X-ray computed tomography, diffuse optical tomography (DOT), denoising, deconvolution problems. Application to experimental sparse CT data and simulated data with different types of noise are performed to further validate the proposed method.

Key words. level set, PaLS, parametric, reconstruction, tomography, piecewise constant

AMS subject classifications. 65F22, 65F99, 65N21

1. Introduction. Inverse problems are of significant interest across a broad range of science and engineering applications, as we detail below. The primary objective of an inverse problem is to extract the unknown composition and structure of a medium based on a set of indirect observations which are related to the unknown via a physical model. In many cases, a detailed map of the medium is either not possible or not needed. Rather, one seeks the identification and characterization of “regions of interest” (ROIs), such as an cancerous tumors from diffuse optical data [5, 71, 79], subsurface contaminants from hydrological data [3, 28, 78] or buried objects from electromagnetic data [17, 20, 55, 59]. These problems are often solved by first forming an image and then post-processing to identify the ROIs [60]. Although this two-step approach can be effective, it is computationally expensive. Moreover, for problems where data are limited, the initial image formation stage will require potentially complex regularization methods to overcome the ill-posed nature of these problems. Alternatively one can use the data to directly estimate the geometry and contrasts of the ROIs [18, 41, 43]. These *shape-based* methods are usually better-posed compared to pixel-based problems; however, topologically complicated and discontinuous shapes can lead to challenges [63]. For example, approaches based in using parametric shapes (circles, ellipsoids, etc.) to describe object geometry require that the number of components for the shape should be *a priori* known or somehow estimated. For this and many other reasons [2], level set methods have found great use for shape-based inverse problems because of their ability to naturally recover objects whose topology (number of connected components) is not known *a priori*.

Level sets methods were first introduced for modeling the propagation of curves by Osher and Sethian [57]. The use of these models for solving inverse problems was initially proposed by Santosa [63] followed by significant subsequent effort based on classical level set evolution methods [9, 24, 31, 42], most notably for image processing applications [16, 62, 72]. For ill-posed inverse problems regularization of the level set function is required. A number of techniques have been considered to address this complication including

conventional pixel-based methods [23], geometric constraints [58] or by choosing the level set functions to be members of finite-dimensional spaces of basis functions such as the the parametric level set function (PaLS) idea first considered for inverse problems by [2]. This latter approach is the basis for the work in this paper.

The PaLS model proved to be capable of capturing the topological advantages of a level set function while avoiding difficulties such as the need for explicit regularization and reinitialization that occur frequently when using traditional level set methods for inverse problems. Moreover, it was shown in [2] that the low order representation of the inverse problem makes it possible to use Newton and quasi-Newton methods for determining the PaLS parameters. In recent work, the PaLS model in [2] and variants have been used across a range of application areas and imaging modalities including geophysics [52, 53] and reservoir monitoring [34, 35], image segmentation [54], acoustic scattering [21], dynamic tomography [56], dual-energy computed tomography [64], electrical impedance tomography [49, 50], electromagnetic imaging [36], electrical capacitance tomography [47], and multi-modal imaging [26].

Despite the advantages of PaLS, there remains a number of areas where improvement is required. One important limitation of existing PaLS models (indeed most all level set methods) is the ability to recover media with one two contrast values using a single level set function. Existing level-set based approaches for multi-contrast, multi-object problems, such as the colour level set [33], vector level set [80], and binary level set [48], either use N level sets for N objects [12, 54, 80] or $\log N$ level sets for N objects [33, 48, 73]. As a result, with the existing methods, as the number of objects with different contrast values increases, the required number of level sets also increases. A second area of limitation for PaLS concerns the family of basis functions used to model the level set function. In a traditional PaLS setting, the level set function is obtained using a weighted superposition of a set of predetermined collection of basis functions, most often radial basis functions (RBFs) [21, 36, 47, 49, 50, 56, 64] but also polynomials [40], multiquadrics [54], ellipsoidal [26], and polytopes [54]. We focus here on RBFs due to their prevalence as well as a some nice properties specifically of compactly supported RBFs [2]. RBFs possess only circular cross sections and thus can limit the range of objects that can be represented by the model and a given number of RBFs. Finally, as effective as they are, the traditional PaLS models still suffer from numerical conditioning issues [2]. PaLS models which adopt RBFs can experience non-uniqueness of parametric representation of shapes due to the fact that infinitely many pairs of parameters can give the same circular cross sections. This defect can end up with poorly conditioned Jacobian matrices (sometimes singular) which we illustrate empirically in this paper. Since the performance of quasi-Newton methods tends to be highly dependent on the condition number of the Jacobian matrix evaluated at each iteration, when quasi-Newton methods are used for the numerical solution of the inverse problems, most of the traditional PaLS models suffer from ill-conditioning of the Jacobian matrices [2].

In this paper, we develop Parametric Level-Sets Enhanced to Improve Reconstitution (PaLEnTIR) for piecewise constant image reconstruction to address the following issues identified above:

- **Multi-contrast:** Most importantly, we replace the binary Heaviside function used in the traditional PaLS models with a smooth transition function in the new model. This way, the new model can capture multiple unknown contrasts with only a single level-set function. To the best of our knowledge, the proposed approach is the first PaLS model that is capable of producing multiple objects each possessing different contrast values with a single level set function. The benefit of this aspect of our model is that the number of parameters to be learned does not change when we want to produce multi-contrast images unless the number of basis functions increases. Moreover, our enhanced PaLS model does not require the explicit estimation of the contrast coefficient parameters. Rather we demonstrate the ability to determine these quantities automatically based on upper and lower bounds on the contrasts over a coarse spatial partition of the imaging region. An iterative process is provided for determining these bounds and the geometric parameters of the PaLS model.
- **Shape expressiveness:** We replace the RBFs used in previous PaLS [2] with anisotropic basis functions which yields basis functions that are capable of producing rotated ellipsoidal cross-sections. As a result, the new basis functions provide greater geometric flexibility and capture much more detail especially for sharp or flat and long objects with which RBFs have difficulty. Consequently, the new PaLS model is capable of recovering more complex objects with fewer basis functions compared to the previous model which use RBFs.
- **Numerical Behavior:** We demonstrate empirically that our new approach of bounding the coeffi-

cients used in the anisotropic basis functions of the PaLS function in addition to fixing the centers of the basis functions in our new model significantly improves the numerical performance of the method. Specifically, the conditioning of the Jacobian matrices is seen to decrease and the convergence of the optimization method for estimating the PaLS parameters is observed to increase.

The organization of the paper is as follows. In Section 2, we define our problem of interest and briefly review the previous parametric level set method [2] for shape-based problems. In Section 3, PaLEnTIR formulations for both 2D and 3D inverse problems are detailed. Here we discuss the benefits of the new formulation relative to existing PaLS models. Our recursive approach for determining the bounds on the contrasts of the ROIs is given in Section 3.1. We provide experimental results for PaLEnTIR in Section 4. Specifically, from Section 4.1 to 4.3, we show the results for a collection of linear 2D problems including denoising, deconvolution, inversion of the Radon transform. In Section 5.1, we demonstrate the performance of PaLEnTIR on a 3D limited view parallel beam tomography experiment. To test our approach on a nonlinear problem, we show the experimental results of the new approach on diffuse optical tomography (DOT), a nonlinear inverse problem, in Section 5.2. Across this range of experiments, we use both real and synthetic data and consider different types of noise such as additive and multiplicative noise as well as data following Poisson statistics to show the robustness of our approach in a range of data-limited applications. Conclusions and future work are provided in Section 6.

2. Problem formulation. We begin by reviewing both inverse problems in general as well as the traditional formulation of the PaLS model.

2.1. Forward and Inverse Problems. Consider a region of space to be imaged defined as $\Omega \in \mathbb{R}^2$ or \mathbb{R}^3 . For \mathbf{r} a point in Ω , let us define a spatially-dependent property $f(\mathbf{r})$ of the medium (e.g., electrical conductivity, optical absorption, sound speed, etc.) which we seek to recover and which belongs to a space of functions, denoted \mathbb{F} . We denote with \mathcal{M} the map which takes $f(\mathbf{r})$ to a vector of noise free data. In many cases, \mathcal{M} encompasses the physics of the sensing modality as well as the engineering details of the particular sensors used to collect the data. In Section 4 we detail the models underlying our examples. In practice, the data available for processing is equal to $\mathcal{M}(f)$ corrupted in some manner by noise. While many noise models are possible, here we consider only the case of additive white Gaussian noise which results in a least squares type of problem although in Section 4 we do demonstrate the ability of our approach to handle data with alternate sources of stochasticity. In summary, the forward model can be written

$$(2.1) \quad \mathbf{d} = \mathcal{M}(f(\mathbf{r})) + \mathbf{w}, \quad \mathbf{d} \in \mathbb{C}^N,$$

where \mathbf{w} represents the additive noise.

The inverse problem requires determination of the unknown property $f(\mathbf{r})$ based on the observed data \mathbf{d} . Following the penalized likelihood approach, (2.1) leads to the following minimization problem as the basis for recovering $f(\mathbf{r})$ from \mathbf{d} ,

$$(2.2) \quad \hat{f} = \arg \min_f \frac{1}{2} \|\mathcal{M}(f) - \mathbf{d}\|_2^2 + \xi(f).$$

The first term $\frac{1}{2} \|\mathcal{M}(f) - \mathbf{d}\|_2^2$ arises from the Gaussian assumption on the noise and quantifies the mismatch error between model prediction and the data. The second term $\xi(f)$ is the regularization functional which incorporate prior information into the minimization problem and imposes a cost on the objective function. This latter term is usually used when the problem is ill-posed and should be chosen based on properties of the problem and prior knowledge concerning e.g., the degree of smoothness associated with f [1, 27, 70]. It is also possible to regularize the problem using a geometric parameterization of the unknown property. This is done by either embedding the regularization implicitly in the parameterization of the unknown property in which case no explicit ξ may be needed or by expressing as geometric constraints on the shape of the unknown [24, 75]. In this paper, we follow the former approach using a PaLS type of model.

2.2. Parametric Level set methods. For the problems of interest in this paper, $f(\mathbf{r})$ consists of two types of regions; object, O , and background, $\Omega \setminus O$ and is written as

$$(2.3) \quad f(\mathbf{r}) = f_O(\mathbf{r})\chi_O(\mathbf{r}) + f_B(\mathbf{r})(1 - \chi_O(\mathbf{r})) \in \mathbb{R}$$

where $f_O(\mathbf{r})$ and $f_B(\mathbf{r})$ are the generally space dependent property values of the object and background respectively and $\chi_O(\mathbf{r})$ is the characteristic function of the region O :

$$\chi_O(\mathbf{r}) = \begin{cases} 1 & \mathbf{r} \in O \\ 0 & \mathbf{r} \in \Omega \setminus O. \end{cases}$$

Under this model, the problem is to find O (or in some cases the boundary, ∂O), as well as the property values in each region. A common simplifying assumption is that both f_O and f_B are constants [69] in which case the focus of the problem is on the recovery of O which in general can be multiply connected with each component having no specific (i.e., easily parameterized) shape. Due to the complicated topology of O , level set methods have proven convenient [2]. Mathematically, the level set representation of the shape of the domain D satisfies

$$(2.4) \quad \phi_O(\mathbf{r}) \begin{cases} < c & \mathbf{r} \in O^{int} \\ = c & \mathbf{r} \in \partial O \\ > c & \mathbf{r} \in \Omega \setminus O \end{cases}$$

where c is a constant that determines the desired level set¹, O^{int} is the interior of the set O and ∂O its boundary [2]. In terms of ϕ_O , the characteristic function of O is written as $\chi_O(\mathbf{r}) = H(\phi_O(\mathbf{r}) - c)$ where $H(x)$ is the Heaviside function which is equal to one for x positive, zero for x negative and $1/2$ for $x = 0$. Thus, (2.3) can be expressed as

$$(2.5) \quad f(\mathbf{r}) = f_O H(\phi(\mathbf{r}) - c) + f_B (1 - H(\phi(\mathbf{r}) - c))$$

where f_O and f_B are the now constant property values of the foreground and background respectively.

Most of the traditional methods follows a finite difference discretization of the level set function which requires a dense collection of nodes. The difficulty of implementing this approach as well as the numerical considerations of discrete computation overshadow the advantages of the level set function especially in the case of ill-posed inverse problems [2, 9]. Alternatively, a parametric form for the level set function can be used for which $\phi_o(\mathbf{r})$ is spanned by a set of basis functions (e.g polynomial, radial basis function, trigonometric, etc). Specifically, the original parametric level set function representation takes the form

$$(2.6) \quad \phi_{og}(\mathbf{r}; \mathbf{p}) = \sum_{j=1}^N \alpha_j \psi(\|\beta_j(\mathbf{r} - \chi_j)\|), \quad \mathbf{p}^T := [\alpha^T \ \beta^T \ \chi^T].$$

In this case the PaLS level set function is formed as a weighted summation of N basis functions $\psi_j(\mathbf{r}) := \psi(\|\beta_j(\mathbf{r} - \chi_j)\|)$ for $j = 1, 2, \dots, N$. The $\psi_j(\mathbf{r})$ are often taken to be RBFs [21, 26, 36, 47, 49, 50, 56, 64]. We will refer to use of such basis functions as “traditional PaLS,” and it is against such representations that we compare our new PaLEnTIR representation.² Each basis function $\psi_j(\mathbf{r})$ is associated with its own dilation coefficient β_j , and center location χ_j . The length $4N$ (for 2D problems) or $5N$ (for 3D) vector \mathbf{p} holds the unknowns to be determined including the vectors α, β , and χ containing the expansion coefficients α_j , the dilation values β_j , and PaLS centers $\chi_j \in \mathbb{R}^2$ or \mathbb{R}^3 respectively.

Combining (2.6) with (2.5), we obtain $f = f(\mathbf{r}, \mathbf{p})$. The goal of a PaLS-based inverse problem is to recover the unknown \mathbf{p} based on the observed data \mathbf{d} and the known physical model \mathcal{M} . In practice, this

¹This could be taken to be the zero level set, though in [2], the case was made for c slightly larger.

²The use of the word “traditional” here is a bit of a misnomer in the following regard: in the paper [2] in which the term “PaLS” was coined, the norm in the argument is replaced by a pseudo-norm and $\psi(\cdot)$ is taken to be a compactly supported radial basis function. Subsequent papers (e.g. [26]) have also built on CSRBF-based PaLS in the context of image reconstruction. The compactness of the basis functions may be advantageous from the point of view that the Jacobian may become sparse, for reasons described in [2]. The basis functions are similar in shape, representing symmetrical spherical bump functions. In the present work, however, we will use Gaussian RBFs instead of CSRBFs and forgo compactness in favor of retaining a norm, rather than a pseudo-norm. This choice facilitates the comparative analysis of the expressiveness and numerical properties of the proposed approach over the so-called traditional approach. However, we note that the parameterization we develop in this paper, as well as the analysis, can be utilized in a CSRBF framework as well.

requires replacing the exact Heaviside function with a differentiable approximation (we discuss this more in section 3.1). If the contrast coefficients f_O and f_B are known, the resultant inverse problem formulation using PaLS takes the form

$$(2.7) \quad \hat{\mathbf{p}} = \arg \min_{\mathbf{p}} \frac{1}{2} \|\mathcal{M}(f(\mathbf{r}, \mathbf{p})) - \mathbf{d}\|_2^2.$$

In the event where the contrasts are not known, a cyclic descent method is often employed [25, 31, 74] in which one alternatively estimates \mathbf{p} for using current estimates of f_O and f_B and then updates the contrasts using the just-computed PaLS parameters. A closed form expressions can be used for the latter problem, the bulk of the algorithmic effort is devoted to estimation of \mathbf{p} . This is a non-linear least squares optimization problem. We will discuss how to solve this non-linear least squares problem in Section 3.2.

Note that the PaLS parameterization gave us the ability to remove the regularization functional $\xi(f)$. This is due to the fact that we have regularized the problem through the parameterization as the number of PaLS basis functions is always much smaller than the size of the grid obtained from discretizing Ω .

3. Parametric Level-sets Enhanced To Improve Reconstruction (PaLEnTIR). In Section 2, we defined the problem using the original PaLS representation shown in (2.6). In this section, we introduce our new PaLS model, called Parametric Level-sets Enhanced To Improve Reconstruction (PaLEnTIR) and we discuss its advantages compared to the original representation. Making explicit the dependence of $f(\mathbf{r})$ on the parameter vector \mathbf{p} , the proposed PaLEnTIR model is defined as follows

$$(3.1) \quad f(\mathbf{r}; \mathbf{p}) = C_H(\mathbf{r})T_w(\phi(\mathbf{r}; \mathbf{p}) - c) + C_L(\mathbf{r})(1 - T_w(\phi(\mathbf{r}; \mathbf{p}) - c))$$

$$(3.2) \quad \phi(\mathbf{r}; \mathbf{p}) = \sum_{j=1}^N \sigma_h(\alpha_i) \psi(\mathbf{R}_j(\mathbf{r} - \chi_j)) \quad \mathbf{p}^T := [\boldsymbol{\alpha}^T \boldsymbol{\beta}^T \boldsymbol{\gamma}^T].$$

where, as explained shortly, the N matrices \mathbf{R}_j for $j = 1, 2, \dots, N$ each depend on subvectors of $\boldsymbol{\beta}$ and $\boldsymbol{\gamma}$ respectively. Comparing (2.6) and (3.2), the PaLEnTIR model differs from the traditional PaLS method in a number of ways designed to address the shortcomings of the original approach to parametric level sets, each of which is discussed in depth in the following sections:

1. **Multi-contrast, single level set** reconstructions are obtained by:
 - (a) Replacing the Heaviside function with the smooth transition function $T_w(x) \in [0, 1]$.
 - (b) Relabeling and reinterpreting $f_O(\mathbf{r})$ and $f_B(\mathbf{r})$ as upper and lower contrast bounds, $C_H(\mathbf{r})$ and $C_L(\mathbf{r})$.
2. **Shape-expressiveness** is expanded by replacing the scalar dilation coefficient, β_j by a matrix \mathbf{R}_j implementing what we are calling stretching and sliding. For 2D problems, each \mathbf{R}_j depends on one element of $\boldsymbol{\beta}$ and one of $\boldsymbol{\gamma}$. In the 3D case, this changes to three β 's and three γ 's.
3. **Numerical performance** is improved by
 - (a) Fixing the basis function centers on a grid of pre-specified points, χ_j so that these quantities are no longer estimated as part of the inversion process, and combined with the new parameterization, reducing the dimension of the search space with fewer number of parameters.
 - (b) Constraining the size of the expansion coefficients using a $\sigma_h(\alpha_i) \in [-1, 1]$ defined in (3.13).

In the remainder of this section we discuss the manner in which the model addresses each of these three issues in turn. For the sake of visualization, we focus on the 2D case; however, the ideas carry over to 3D which will be explored in Section 5.1.

3.1. Multi-contrast, Single Level Set Reconstructions. In the previous section, we assumed that the property function $f(\mathbf{r})$ had a binary structure, i.e. each point in Ω either belongs to the region O or the background. However, it may well be the case that we have to represent regions containing objects with more than two contrast values [4, 32, 51, 66, 76]. To solve this problem, we replace the Heaviside function in the original PaLS model with a transition function $T_w(x)$ which smoothly, and monotonically varies from zero and one. Specifically, in this paper we take

$$(3.3) \quad T_w(x) = \frac{1}{2} \left[1 + \frac{2}{\pi} \tan^{-1} \left(\frac{\pi x}{w} \right) \right]$$

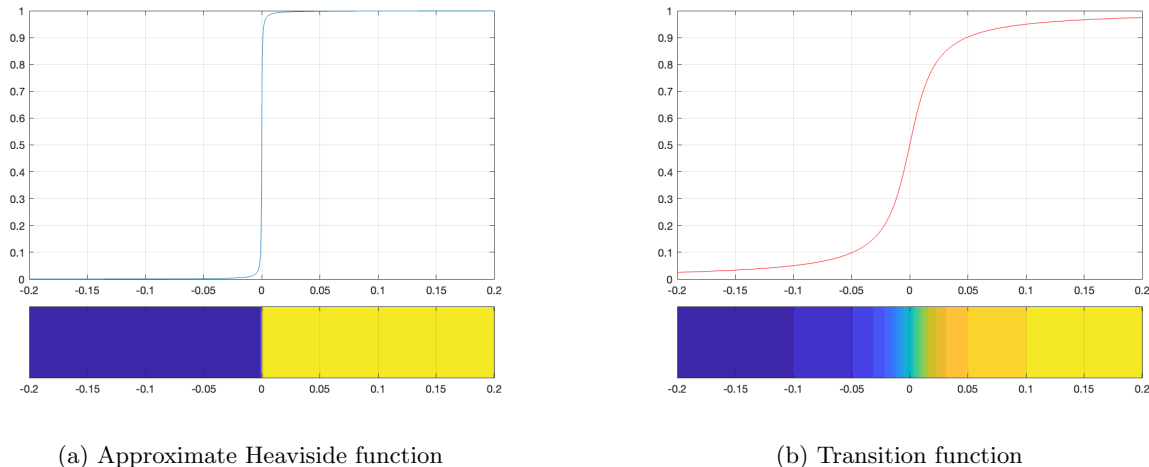
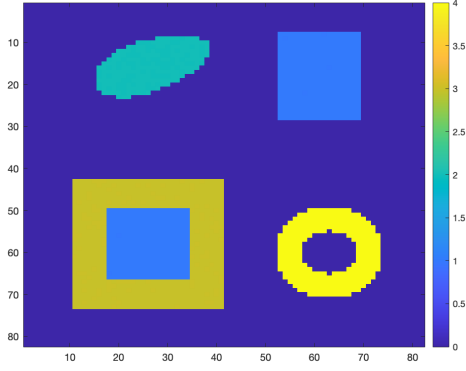


Fig. 3.1: Comparison of the old approximate Heaviside function and the new transition function in the proposed model

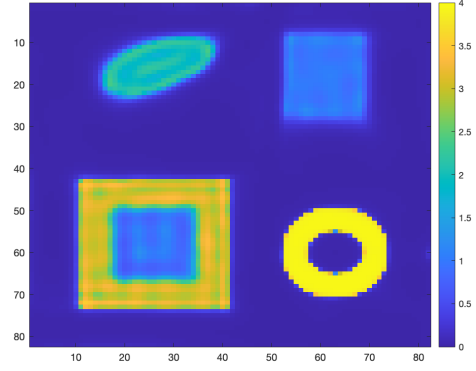
where w determines the steepness of the transition region. It is certainly the case that the approximate Heaviside function used in the original PaLS work also monotonically increased from zero to one [2] and thus is similar to T_w . The difference lies in the width of the transition. As seen in Figure 3.1a, for the approximate Heaviside, the transition region is by construction very narrow as the goal was to represent binary valued objects whose “phases” are separated by a narrow diffuse interface. In the new formulation, we increase w to stretch the width of this transition region so that, from (3.1), $f(\mathbf{r})$ can assume basically *any* value between $C_L(\mathbf{r})$ and $C_H(\mathbf{r})$ as seen in Figure 3.1b.

To illustrate the impact of these changes to the PaLS model, in Figure 3.2a we display an image comprised of four piecewise constant objects on a zero-contrast background along with our PaLenTIR reconstruction in Figure 3.2b. In this case we took the forward model to be the identity so that $\mathbf{d} = \mathbf{f}(\mathbf{p}) + \mathbf{w}$ and \mathbf{w} is vector of independent identically distributed Gaussian random variables common variance such that the signal to noise ratio (SNR) is 40 dB. Thus, the estimate of \mathbf{p} was chosen to minimize $\|\mathbf{d} - \mathbf{f}(\mathbf{p})\|_2^2$. We used 121 basis functions centered on an equally spaced 11×11 grid. We chose the upper and lower contrast coefficients, $C_H(\mathbf{r})$ and $C_L(\mathbf{r})$, as 4 and 0 respectively since the maximum contrast in the image is equal to 4 and minimum is equal to 0 which belongs to the background. Details of the optimization methods used to solve for \mathbf{p} are provided in Appendix. The mesh plot in Figure 3.2c displays $\phi(\hat{\mathbf{p}})$; that is, the input to $T_w(\cdot)$, which yields the PaLenTIR reconstructed image in Figure 3.2b. We see that the bright yellow region, whose contrast is equal to C_H , is recovered most accurately. The basis function series in this case takes on relatively large values which are truncated by T_w . The regions where there is no object also look very rough in the mesh plot; however in those areas the basis function series is negative so that the transition function T_w creates a constant, zero-background. Looking at both $\mathbf{f}(\hat{\mathbf{p}})$ as well as the 1D plots of the cuts through the rows 16 and 62 of the recovered images in Figure 3.2d and 3.2e we see mixed results. Both the edges and the contrast of the outer ring in the lower right square annular object with contrast close to the maximum of 4 are accurately recovered. For the remainder of the structures whose contrasts are between 0 and 4, we see blurred edges and oscillations in the contrast that are not dissimilar from what we would expect from least squares denoising.

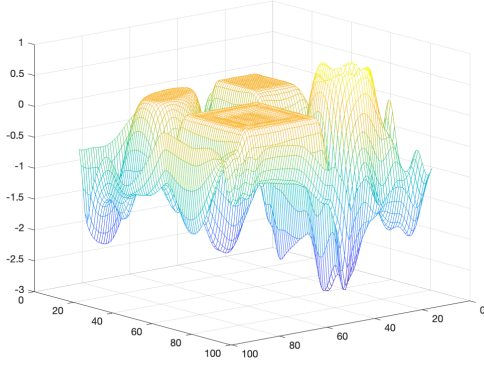
The strong results in Figure 3.2b in the case of the background and the object in the lower right corner arise from the ability of the transition function to truncate the values of ϕ which are not between C_H and C_L . More generally, PaLenTIR can achieve similar results across the the entire scene by setting $C_H(\mathbf{r})$ and $C_L(\mathbf{r})$ in a space varying manner. The key issue here of course is to do this in a manner which retains the advantages of a PaLS-type of approach; namely low order and no need for explicit regularization. To motivate



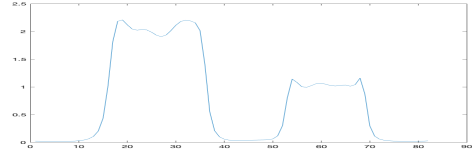
(a) Original image



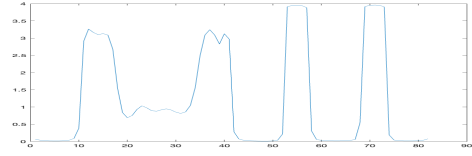
(b) PaLEnTIR reconstruction



(c) Mesh plots of the basis function series



(d) Cut of recovered objects through row 16



(e) Cut of recovered objects through row 62

Fig. 3.2: Experiment results of multi-contrast object recovery using PaLEnTIR . (c) Mesh plot and (d,e) cuts of recovered objects through rows 16 and 62 are shown to illustrate the behavior of the basis functions in the new formulation with the transition function.

our adaptive approach for setting these parameters discussed in Section 3.1, in Figure 3.3 we display a series of three reconstructions where we update the contrast limits iteratively by hand, according to the previous results. Let us assume that, for the reconstruction in the first row of the figure, we have the information of the contrasts of the ellipsoidal, square and doughnut-shaped objects and their rough locations from e.g., the results in Figure 3.2b. We use this “prior knowledge” to manually adjust the C_H values to those in Figure 3.3b. The resulting PaLEnTIR reconstruction obtained by using these values of $C_H(\mathbf{r})$ and $C_L(\mathbf{r})$ to estimate \mathbf{p} is shown in Figure 3.3c and recovers the blue square and green ovoid with the same fidelity as the yellow annulus from before. For the reconstructions in the second and third rows of the figure, we update first the C_H in the second reconstruction in Figure 3.3e and then the C_L in Figure 3.3g according to the gathered information from the first reconstruction about the location and the contrasts of the nested objects and obtain similar results for the square annulus. The PSNR values of the three PaLEnTIR images are respectively 31.66dB, 34.45dB and 37.20dB .

The results in Figure 3.3 and the associated discussion illustrate the ability of the PaLEnTIR model to recover piecewise constant scenes comprised of objects with more than two contrasts using a single level set function. This feature and its practical utility rest heavily on the ability to specify space-varying bounds

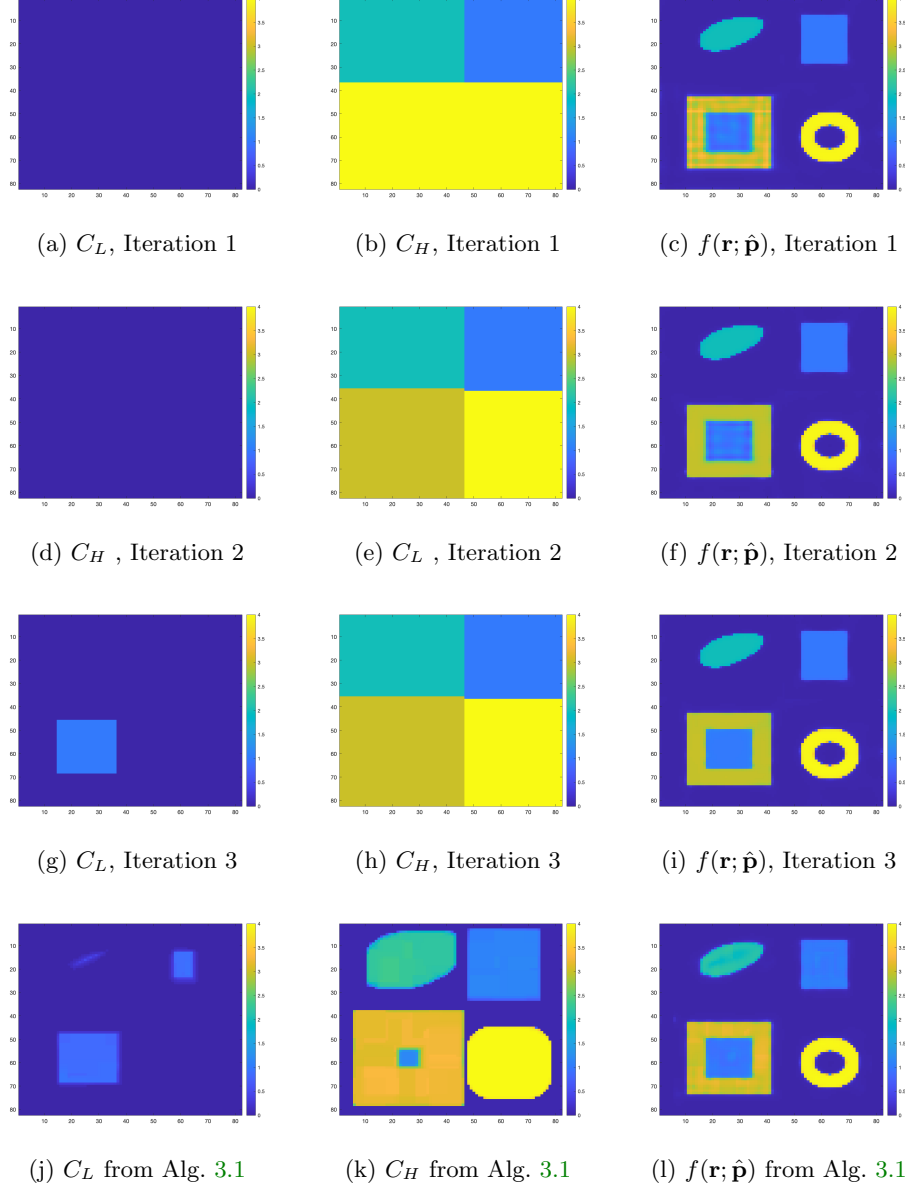


Fig. 3.3: PaLEnTIR Reconstructions of the same objects in Figure 3.2a. (a) - (i) Starting with the reconstruction in Figure 3.2b, $C_L(\mathbf{r})$ and $C_H(\mathbf{r})$ are manually updated over three iterations as described in the text. (j)-(l) PaLEnTIR reconstruction using Algo. (3.1).

on the contrasts at relatively coarse scales. Indeed the need to recover anything approaching “pixelated” versions of these function would nullify any advantages of a PaLS-type approach to inversion. Here we propose an iterative algorithm, shown in algorithm 3.1, to automatically set each $C_H(\mathbf{r})$ and $C_L(\mathbf{r})$ in a deterministic way without abandoning the advantages of PaLS. We begin by initializing the $C_H(\mathbf{r})$ and $C_L(\mathbf{r})$ as constants. The best performance is achieved when C_H and C_L are initialized to the maximum and minimum contrast values of the desired image. We have found that the ultimate performance is not terribly sensitive to the precise choices here. In each iteration, we start by solving the non-linear least squares problem shown in (4.2) using the current values for $C_H(\mathbf{r})$ and $C_L(\mathbf{r})$. An estimate of the image is then

obtained as $f(\mathbf{r}; \hat{\mathbf{p}}^{(k)})$. Using the solution of the non-linear least squares problem, $C_H(\mathbf{r})$ (resp. $C_L(\mathbf{r})$) is updated to the maximum (resp. minimum) value of $f(\mathbf{r}; \hat{\mathbf{p}}^{(k)})$ within a window centered at \mathbf{r} and size of δ . If the relative change of either $C_H(\mathbf{r})$ or $C_L(\mathbf{r})$ for a given \mathbf{r} is less than a threshold, say 2%, then the algorithm skips the update. This rule is not mandatory and if it is removed, the algorithm still converges. The reason for us to use this rule is rather practical, we observed that the algorithm converges much faster and to a better objective score. The algorithm converges and stops when either relative changes in all of the low and high distributions are below the threshold, 2% in this paper, or relative decrease in the residual norm drops below a small threshold, ρ in algorithm 3.1, or the residual norm drops below the error tolerance, κ in algorithm 3.1.

Algorithm 3.1 Algorithm for updating $C_H(\mathbf{r})$ and $C_L(\mathbf{r})$

```

 $C_L(\mathbf{r}) = C_{\min}$  and  $C_H(\mathbf{r}) = C_{\max}$ 
 $\hat{\mathbf{p}}^{(-1)} = \infty$ 
 $\mathbf{F}^{(-1)} = \infty$ 
 $k = 0$ 
while  $\frac{\|\mathbf{F}^{(k-1)} - \mathbf{F}^{(k)}\|_2^2}{\|\mathbf{F}^{(k-1)}\|_2^2} \geq \rho$  or  $\|\mathbf{F}^{(k)}\|_2^2 > \kappa$  do                                 $\triangleright \rho$ : small threshold,  $\kappa$ : error tolerance
     $k = k + 1$ 
     $\mathbf{F}^{(k)} = \mathcal{M}(f(\mathbf{r}, \mathbf{p})) - \mathbf{d}$ 
     $\hat{\mathbf{p}}^{(k)} = \arg \min_{\mathbf{p}} \frac{1}{2} \|\mathbf{F}^{(k)}\|_2^2$                                  $\triangleright$  Using  $C_H(\mathbf{r})$  and  $C_L(\mathbf{r})$ 
    if  $\frac{C_L(\mathbf{r}) - C_L(\mathbf{r})}{C_L(\mathbf{r})} > \eta$  then                                 $\triangleright$  Do not update if the relative change is below a threshold  $\eta$ 
         $C_L(\mathbf{r}) = \min_{\mathbf{r} \in W_\delta(\mathbf{r}_0)} (f(\mathbf{r}_0; \hat{\mathbf{p}}))$                                  $\triangleright W_\delta$ : window size
    end if
    if  $\frac{C_H(\mathbf{r}) - C_H(\mathbf{r})}{C_H(\mathbf{r})} > \eta$  then                                 $\triangleright$  Do not update if the relative change is below a threshold  $\eta$ 
         $C_H(\mathbf{r}) = \max_{\mathbf{r} \in W_\delta(\mathbf{r}_0)} (f(\mathbf{r}_0; \hat{\mathbf{p}}))$                                  $\triangleright W_\delta$ : window size
    end if
end while

```

Figure 3.3(j)-(l) shows the reconstructed image using the method as well as the final contrast coefficients. We started the first reconstruction with uniform contrast coefficients, $C_H = 4$ and $C_L = 0$. The C_H and C_L parameters converged after the third iteration to those in Figure 3.3j and 3.3k. The PSNR of the reconstructed image improved significantly compared to the previous reconstruction in Figure 3.2, from 28.71dB to 34.93dB to be compared with the PSNR of 37.20dB in Figure 3.3i which was obtained assuming the bounds were known *a priori*.

3.2. Advancements in the shape-expressiveness. Radial basis functions (RBFs) provide flexibility in representing a large class of shapes and they are very commonly used in PaLS methods. The RBF formulation is capable of reconstructing the shapes with a very small number of terms in a PaLS representation. However, there are some drawbacks of this formulation. One of the issues is that it can only produce circular cross-sections. For certain classes of shapes, such as one that are highly anisotropic, the use of circular cross sections is inefficient [26]. It is also stated in [26] that in 3D models that adopt RBF representation, such as in [45], that is restricted spherical cross sections, results in limited expressiveness and spherical effects in the reconstructed objects. For more detail, the comparison of the RBFs and ellipsoidal basis function representations on a 3D problem can be found in [26]. Motivated by these observations, we replace the RBFs in the old PaLS [2] with a model of the form

$$(3.4) \quad \psi(\mathbf{r}) = e^{-\|(\mathbf{R}(\mathbf{r}-\mathbf{x}))\|_2^2},$$

where \mathbf{R} will be 2×2 for 2D problems and 3×3 for 3D problems. As in [26], this model produces elliptical cross sections however the parameterization of \mathbf{R} is new.

2D Stretch and Slide Matrix. In the 2D case we define

$$(3.5) \quad \mathbf{R} = \mu \begin{bmatrix} e^\beta & \gamma \\ 0 & e^{-\beta} \end{bmatrix}$$

9

We will discuss the shape expressiveness of the new model over the level set representation of $\phi(\mathbf{r}, \mathbf{p})$ in (3.2) for $N = 1$ case. Let us first define *c-level* set representation of a curve Γ as $\Gamma = H(\phi(\mathbf{r}, \mathbf{p}) - c)$. The curve Γ is identified with the *c*-contour of the function ϕ , i.e Γ is formed from the junction of points \mathbf{r} that gives $\phi(\mathbf{r}, \mathbf{p}) = c$. So we can define Γ for 2D as,

$$(3.6) \quad \Gamma = \{(x, y) | \phi(x, y, \mathbf{p}) = c\}.$$

Before the discussion of the new parameterization, let us first examine the *c-level* representation of a PaLS formulated by a single RBF centered at the origin. We can define this PaLS function, ϕ_{rbf} , as

$$(3.7) \quad \phi_{rbf}(x, y, \alpha, \beta) = \alpha e^{-\beta(x^2+y^2)}.$$

If we place ϕ_{rbf} into (3.6), divide both sides with α and take the natural logarithm of both sides (assuming $\frac{\alpha}{c} > 0$ and $c \neq 0$) we get

$$(3.8) \quad \Gamma_{rbf} = \left\{ (x, y) | x^2 + y^2 = \frac{1}{\beta} \ln \frac{\alpha}{c} \right\}.$$

The equation in (3.8) is definition of a circle with a radius of $\sqrt{\frac{1}{\beta} \ln \frac{\alpha}{c}}$. Hence the *c-level* of a PaLS with an RBF can only produce a circular cross section with a radius defined by the parameters α, β . Although c is a fixed constant it plays a decisive role on the radius as well. After this observation, now let us look at the *c-level* representation of the new model for $N = 1$. The new PaLS function for $N = 1$, ϕ_{new} , is defined as

$$(3.9) \quad \phi_{new}(x, y, \alpha, \mathbf{R}) = \sigma_h(\alpha) e^{-([x \ y] \mathbf{R}^T \mathbf{R} [x \ y]^T)}.$$

The function $\sigma_h(\cdot)$ is defined in (3.13). For this section, it is enough to know that $\sigma_h(\cdot)$ is used to bound the weight coefficient of the basis function between -1 and 1 . When we place ϕ_{new} into (3.6), and do the same operations as in the previous case (assuming $\frac{\sigma_h(\alpha)}{c} > 0$ and $c \neq 0$) we get

$$(3.10) \quad \Gamma_{new} = \left\{ (x, y) | e^{2\beta} x^2 + (2\gamma e^\beta) xy + (\gamma^2 + e^{-2\beta}) y^2 = \frac{1}{\mu^2} \ln \frac{\sigma_h(\alpha)}{c} \right\}.$$

The shape formation of the curve Γ_{new} can be divided into 3 categories as follows:

- **Expansion:** When β and γ are 0, similar to Γ_{rbf} , Γ_{new} becomes a circle with a radius of τ where $\tau^2 = \frac{1}{\mu^2} \ln \frac{\sigma_h(\alpha)}{c}$. Here μ is a fixed constant relative to grid spacing. Similar to the constant c , change in μ also has an impact on the radius of the circle. Unlike the Γ_{rbf} , the circle can be expanded by only one parameter, α , whereas for Γ_{rbf} in (3.8), both α and β can expand the circle.
- **Stretching and sliding:** We view \mathbf{R} as the Cholesky factor of the symmetric positive definite (SPD) matrix $\mathbf{A} = \mathbf{R}^T \mathbf{R}$ which we call the *Stretch and Slide Matrix*. This matrix includes two types of parameters which are estimated by the PaLEnTIR reconstruction: the *stretching* parameter β and the *sliding* parameter γ . In Figure 3.4a, the impact of the *stretching* parameter β is shown. Nonzero values of β transform circles into ellipses with principle axes in the cardinal directions. We can imagine the impact of β as someone is holding the the circle (assuming $\beta = 0$ initially) from two opposing points which are touching the either of the cardinal axes (points shown with green dots in Figure 3.4a), and stretching in the direction of green dashed arrows shown in Figure 3.4a. We call this shape transformation “stretching,” and hence β as the *stretching* parameter. Similarly, as shown in Figure 3.4b γ is the *sliding* parameter because γ horizontally “slides” the maximum and the minimum points in the vertical axes of the ellipse as shown in with red dashed arrows. Due to the fact that the determinant of \mathbf{A} is 1, these 2 shape transformations do not change the area of the ellipse. The area depends on constants μ, c , and the parameter α . In summary, α controls the total area by homogeneously expanding the shape, β controls the upper and lower tangent lines by stretching the ellipse, and γ slides the tangent points of the ellipse over the tangent lines.

In comparison to the PaLS formulation with RBF, the proposed formulation adds rotatable ellipses besides circles. Each parameter in the proposed model has its unique influence on the shape unlike the

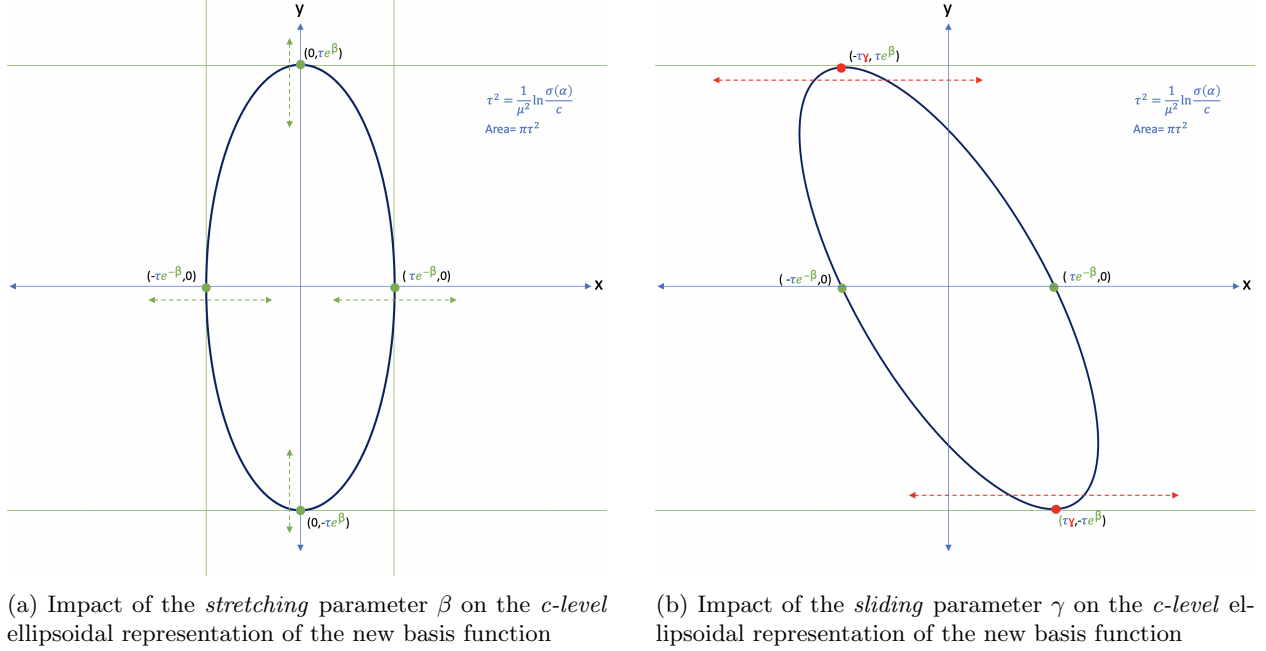


Fig. 3.4: The impact of the parameters on the c -level ellipsoidal representation of the new basis function

RBF formulation in which all parameters can influence the shape in the same way. This contributes to uniqueness of parametric to image mappings. Also the bounded weight coefficients due to function $\sigma_h(\cdot)$ avoids unnecessarily large shapes by a single basis function. We discuss these two outcomes in section 3.3 as an advantage in numerical performance over the RBF formulation.

3D Dilation Matrix. The 3D equivalent $\mathbf{R}_3 \in \mathbb{R}^{3 \times 3}$ for the 3D model is defined in its factorized form as

$$(3.11) \quad \mathbf{R}_3 = \mu \begin{bmatrix} e^{\beta_1} & \gamma_1 & 0 \\ 0 & e^{-\beta_1} & 0 \\ 0 & 0 & 1 \end{bmatrix} \times \begin{bmatrix} 1 & 0 & 0 \\ 0 & e^{\beta_2} & \gamma_2 \\ 0 & 0 & e^{-\beta_2} \end{bmatrix} \times \begin{bmatrix} e^{\beta_3} & 0 & \gamma_3 \\ 0 & 1 & 0 \\ 0 & 0 & e^{-\beta_1} \end{bmatrix}.$$

Note there are 6 parameters, and each of the 3 matrices in the product affects a shear transformation in a 2D plane within \mathbf{R}_3 .

We note that in the 3D PaLS model in [26], the authors do modify the CSRBF formulation to use a matrix-based dilation in order to define ellipsoids. Unlike what we propose here, for the 3D model, their method utilizes a symmetric 3x3 matrix \mathbf{B} instead of $\mathbf{R}_3^T \mathbf{R}_3$ shown as in Eq. 3.12

$$(3.12) \quad \mathbf{B} = \begin{bmatrix} B^1 & B^2 & B^3 \\ B^2 & B^4 & B^5 \\ B^3 & B^5 & B^6 \end{bmatrix}$$

Their method has a more generalized ellipsoidal basis function representation. We propose rather a specific family of ellipses in 2D which are formed by "stretching", "sliding" and "expanding", which we discussed in section 3.2. One of the advantages of our formulation is that the dilation matrix is always symmetric positive definite (SPD). Whereas, in the 3D PaLS model in [26], a regularization is required to ensure that the matrix \mathbf{B} is SPD.

3.3. Numerical improvements and stability. One of the goals of our work in this paper is to find a PaLS parameterization that minimizes the number of parameters required to describe complicated shapes. We also want to improve shape specificity overall. The numerical performance of PaLS methods depend on various issues:

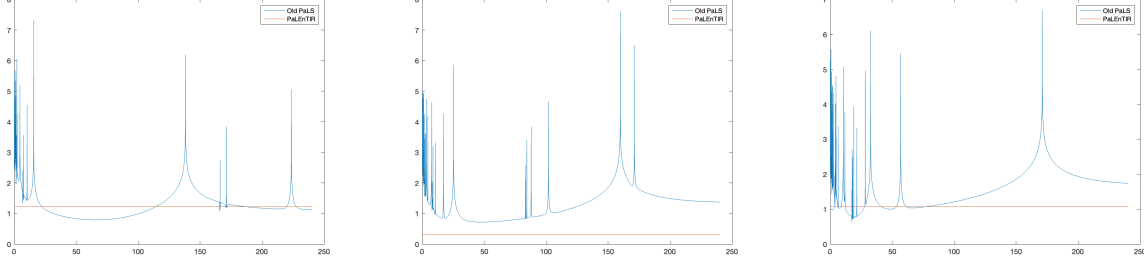
- Total number of parameters (directly related to number of basis functions used, and which PaLS model is employed)
- Sensitivity to parameters. Because the image is formed indirectly from the parameters via application of an approximate Heaviside to the basis function surface, it is possible that a particular basis function does not contribute to the image (this would happen if the amplitude is below the cutoff, or near zero).
- Non-uniqueness of parametric to image mappings. Consider a circle. We can obtain the image of a circle from a single RBF either by suitable changes to dilation or suitable changes to the amplitude. If 2 RBFs are used, they can also be co-located. Likewise, if rotations were employed in 3D, rotation values that achieve the same image are not unique. When RBFs centers can move, the method is also agnostic to which of the RBFs produced the image.

As discussed earlier, the number of parameters in the new model is reduced through the fixed centers and the use of a more flexible basis function formulation compared to old model. The reduction in the number of parameters improves the performance of the numerical methods on the new model. Besides that, the new model puts boundaries to the weight parameters by using the hyperbolic tangent function. Numerically ill-conditioned Jacobian matrices occur in PaLS formulations when differentiating a pixelated image with respect to the basis function parameters. An ill-conditioned Jacobian matrix cause Gauss-Newton and other derivative-based optimization algorithms to compute erroneous descent directions in parameter estimation problems and also increase uncertainty of the parameter estimates [10, 22, 65].

We discovered that the conditioning of the Jacobian worsens as the weight parameters grow in magnitude and approach to infinity. By using the hyperbolic tangent function $\sigma_h(\cdot)$ shown in Eq. 3.13, the weights of the basis function are bounded between -1 and +1 and hence it is not possible for a basis function to take on exponentially large positive and negative values which would produce poorly conditioned Jacobian matrices. Moreover, bounded weight coefficients avoids the possibility of domination of the entire image by a few number of basis functions with large weight coefficients. In such a situation, some of the basis functions can almost be ineffective to the solution. Consequently, changes in the three coefficients of these basis functions have negligible effects on the resulting solution and their associated columns of the Jacobian matrix have small magnitudes. With the bounded weight coefficients and fixed centers, PaLEnTIR encourages each and every basis function to significantly contribute to the solution and hence gives rise to better conditioned Jacobian matrix.

$$(3.13) \quad \sigma_h(\alpha) = \tanh\left(\frac{\alpha}{2}\right) = \frac{1 - e^{-\alpha}}{1 + e^{-\alpha}}.$$

RBF formulation have a non-unique parameter to *c-level* representation mapping, i.e we could produce the same circle from the RBF cross section with many parameter pairs as discussed in section 3.2. We found that this can end up with poorly conditioned Jacobian matrices during the optimization. To illustrate our observation, we compare the conditioning of the PaLS with the RBF formulation and the proposed PaLEnTIR with the new anisotropic basis functions for $N = 1$ case, i.e PaLS functions are formulated as each having a single basis function. Since RBFs are only capable of producing circular cross sections as discussed in section 3.2, we compare each model's conditioning when the both basis functions form the same circle with their *c-level* representation. We picked 3 different radii for this illustration. Figure 3.5 shows the condition numbers of the Jacobian matrices of the both models. We take logarithm with base 10 of the condition number of the models to have a better visualisation. The image grid is from -1 to 1, hence 0.4 diameter corresponds to 20% of the total width of the image. There is a unique parameter pair for the proposed basis function to produce a circular cross section with a specific diameter. Hence there is only a single condition number for PaLEnTIR in each plot, and it is drawn with a red straight line. Whereas for the RBF there are infinitely many parameter pairs. For this reason the horizontal axes of plots in the Figure correspond to α values with which the RBF produced the desired circular cross section. The β values for the RBF are not shown since it can be calculated from the given α and the circle diameter. The condition number of the old PaLS is shown with the blue line over α values between 0.1 to 240. Notice for all 3 examples, the new basis function shows better or similar performance in terms of the condition number. However, RBF shows very poor performance around several α values. In fact, all 3 examples show that at several points, RBF produces singular Jacobian matrices which ends up with infinite condition number(spikes in



(a) Condition number plots for the re- (b) Condition number plots for the re- (c) Condition number plots for the re-
construction of a circle of radius 0.1. construction of a circle of radius 0.16. construction of a circle of radius 0.2.

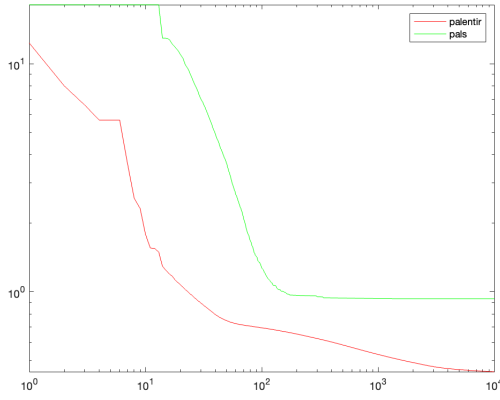
Fig. 3.5: Comparison of Condition number of the Jacobian for Old PaLS and PaLEnTIR . Each figure compare the model’s conditioning when the both models try to produce the same circle with their *c-level* representation. The experiment is repeated for producing 3 circles with different radii. The radii are stated below each plot. The red line represents the PaLEnTIR , and the blue line represents the RBF formulation

the plots). Non-uniqueness of parametric to image mappings of RBFs can give rise to singular Jacobian matrices which can weaken the performance of quasi-Newton methods [2]. The proposed anisotropic basis function formulation prevents this from happening with the unique *c-level* shape representation.

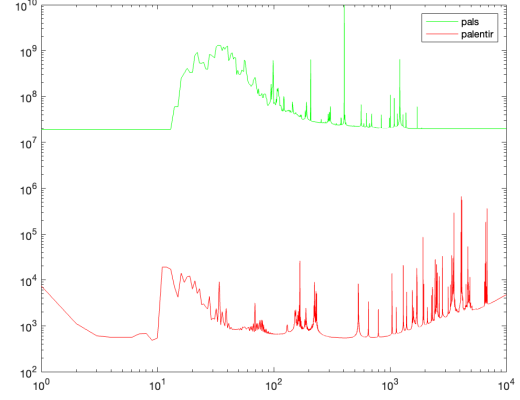
For the numerical comparison of the overall models formulated with more than 1 basis functions, Figure 3.6 plots the residual of the problem and the conditioning of the Jacobian for each iteration during the training of the two aforementioned methods; the new PaLEnTIR , and the PaLS model with the RBF formulations. Notice both plots are in Log-log scale for the sake of a clearer visualization. To solve the nonlinear least squares problem defined in 4.2, we use the TREGS algorithm in [67]. The plots are formed by averaging 100 different runs of the optimizer for a 32x32 image recovery denoising problem. The input of each run is exposed to total of 100 different additive Gaussian noise instances, each with 1% noise level. Each model uses 6x6 RBFs. If we look at Figure 3.6b, clearly, the new model is capable of significantly improving the average conditioning of the Jacobian compared to the old PaLS during the entire TREGS run. In Figure 3.6a we observe the average convergence plots of the two models. PaLEnTIR model manages to converge to a better residual while also maintaining a steeper convergence and better conditioning. The seen improvements in the conditioning in terms of improvement and stability significantly facilitate the use of quasi-Newton methods.

4. Experimental evaluation. We explore the utility of PaLEnTIR using a variety of linear and nonlinear forward models, particularly when the data are limited. All experiments require that we use a discrete form of the forward model developed in Section 2. To keep the discussion simple, we will assume that the forward operator is discretized by a quadrature rule if the forward operator is an integral operator or by finite differences if the forward operator involves a PDE. We could use other methods of discretization, but these assumptions permit a straightforward extension of the continuous to discrete notation for purposes of this paper: that is, the vector of unknowns will represent values of the desired function $f(\mathbf{r})$ at a finite set of grid points. Specifically, suppose that $\mathbf{r}_i, i = 1, \dots, N_{pts}$ denotes a discrete set of points in Ω (i.e. each \mathbf{r}_i represents a 2D or 3D spatial gridpoint). We will define the length- N_{pts} vector $\mathbf{f}(\mathbf{p})$ such that $[\mathbf{f}(\mathbf{p})]_i = f(\mathbf{r}_i; \mathbf{p})$. In this discrete case, $\mathcal{M}(\mathbf{f}(\mathbf{p}))$ represents the measured data for all sources given the discrete values $f(\mathbf{r}_i; \mathbf{p})$. The discrete forward model is thus

$$(4.1) \quad \mathbf{d} = \mathcal{M}(\mathbf{f}(\mathbf{p})) + \mathbf{w}.$$



(a) Plots of average residuals, \mathbf{F} (3.1), over TREGS iterations in Log-log scale.



(b) Plots of average condition number of the Jacobian matrices over TREGS iterations in Log-log scale

Fig. 3.6: Condition number of the Jacobian matrix and the residual \mathbf{F} (3.1) plots over TREGS [67] iterations formed by averaging 100 different TREGS runs with each having a different \mathbf{w} realization. Green line represents old PaLS and red line represents the new PaLEnTIR. Both plots are in Log-log scale.

With this model, the problem of inverting for the unknown parameters that describe the image requires solving a non-linear least squares problem

$$(4.2) \quad \hat{\mathbf{p}} = \arg \min_{\mathbf{p}} \frac{1}{2} \|\mathcal{M}(\mathbf{f}(\mathbf{p})) - \mathbf{d}\|_2^2$$

for which we use the TREGS algorithm [67], a regularized trust-region based approach. For each of the problems below, it suffices to indicate the particular forward mapping $\mathcal{M}(\mathbf{f}(\mathbf{p}))$. Details of the parameter selection and initialization process as well as optimization methods used to solve for $\mathbf{f}(\mathbf{p})$ are provided in Appendix.

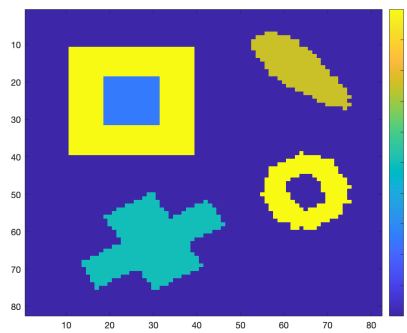
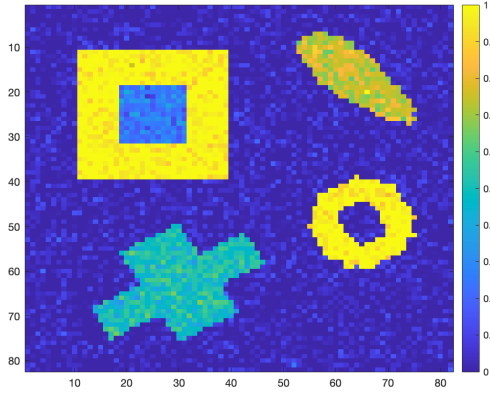
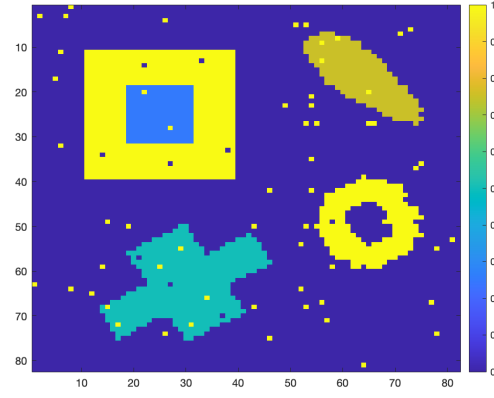


Fig. 4.1: Synthetically generated image of four objects

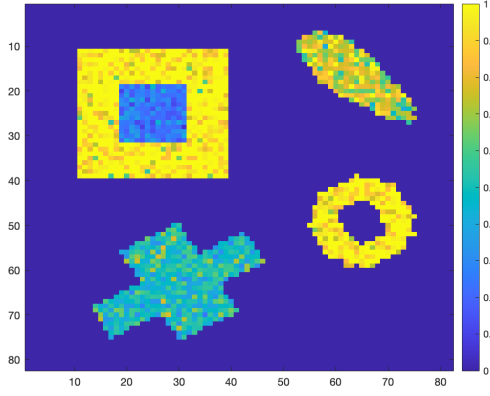
4.1. Denoising. In this paper, the denoising problem requires the solution of (4.2), with the forward mapping $\mathcal{M}(\mathbf{f}(\mathbf{p})) = \mathbf{f}(\mathbf{p})$. We used the synthetic image shown in Figure 4.1 comprised of four objects with a total of five contrast values (including the background contrast) each having a complex geometry (sharp



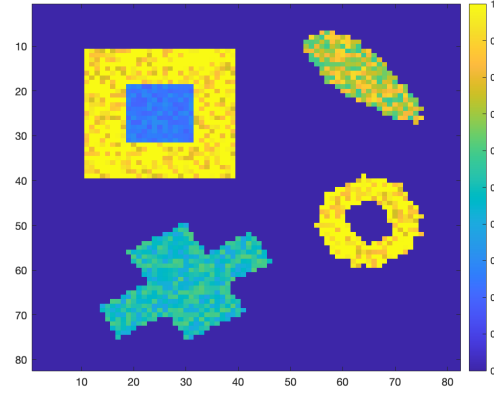
(a) Gaussian noise



(b) Salt and pepper noise



(c) Poisson noise



(d) Speckle noise

SNR values for the experiment data	
Noise Type	Data SNR(dB)
Gaussian Noise	18.87
Salt and Pepper Noise	12.99
Poisson Noise	17.85
Speckle Noise	19.40

Fig. 4.2: Input images, that are exposed to different types of noise, for the denoising experiment are shown. The table shows the corresponding SNR values for each noise type.

edges, nested objects, rotated objects, objects having gap inside). We carried out the experiment with four types of randomness: additive Gaussian noise, salt and pepper noise, multiplicative speckle, and using the true object to generate Poisson data. The resulting data are shown in Figure 4.2. The table in Figure 4.2 shows the data Signal-to-noise ratio (SNR) in decibels of the noisy images. SNR is a measure to quantify the signal quality by comparing the level of a desired signal to the level of noise existing in the data. In this

paper, SNR is calculated as

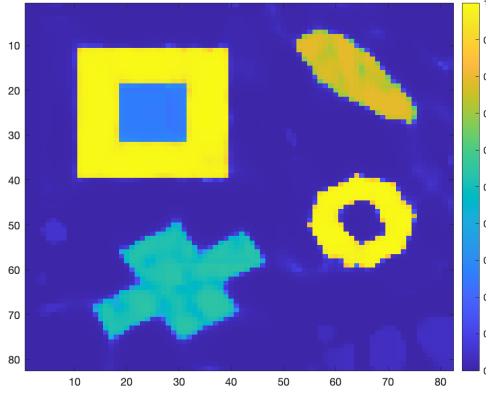
$$(4.3) \quad \text{SNR}_{dB} = 20\log_{10} \left(\frac{\sqrt{\sum_{n=1}^N |x_n|^2}}{\sqrt{\sum_{n=1}^N |w_n|^2}} \right)$$

where x_n and w_n are the n^{th} element of the signal and the noise respectively. For all of the experiments, C_H and C_L in the PaLEnTIR model are initialized as the maximum and minimum values of the whole image and hence 1 and 0 respectively for the experiments whose goal is to reconstruct the image in Figure 4.1. We use 144 basis functions centered on a 12×12 grid resulting in 432 unknowns. This is over an 85% reduction in parameters compared to the 82×82 array of 6724 pixels comprising the underlying discretization of the image domain. We compare the performance of the PaLEnTIR model with that obtained using the L2-Total Variation (TV) regularization [15]. For the parameter selection of the L2-TV regularization, we iterated over 20000 parameter values for each problem and picked the one with the smallest mean square error thereby providing the best possible result from using this approach. Note that, PaLEnTIR does not require an explicit parameter selection procedure. For each of the four cases we compare the both methods according to the following metrics: PSNR (dB), SNR (dB), SSIM, MSE. Structural Similarity Index (SSIM) is a metric that is created to replicate the human visual perception system [77]. The metric compares the two images, the reference image and the one we are interested in, based on three characteristics of an image: luminance, contrast and structure. We use SSIM to reflect visual goodness of an image. A value closer to 1 indicates that the two images are very similar, whereas -1 indicates the opposite. Mean Squared Error (MSE) is a commonly used metric to quantify the difference in the values of each of the corresponding pixels between the sample and the reference images. PSNR is a commonly used metric to quantify the signal quality by comparing the peak level of a desired signal to the level of noise. Both PSNR and MSE are representations of absolute error whereas SSIM gives perception error.

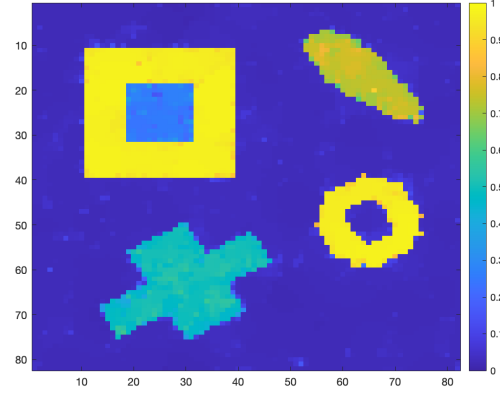
4.1.1. Additive Gaussian Noise. Our first denoising experiment is with the additive Gaussian noise. The input image corrupted with the Gaussian noise is shown in Figure 4.2a. The data SNR of the input is 18.87dB. The L2-TV and the PaLEnTIR reconstructions of the image as well as the table of performance metrics are shown in Figure 4.3. Visually speaking, objects in PaLEnTIR reconstruction are much more homogeneous than the ones in the TV reconstruction. For instance, the nested squares on the top left of the image have very rough surfaces in the TV reconstruction while they are very smooth in PaLEnTIR reconstruction. In both of the reconstructions, there are artifacts in the background. In TV reconstruction there many but small artifacts whereas in PaLEnTIR there are few but larger ones. Since the region of interest in this experiment is not the background, this is not a concerning observation. Even using an omniscient approach to selecting the regularization parameter for the L2-TV method, the PaLEnTIR method is superior for all four of the metrics. In terms of absolute error, PaLEnTIR scored better in SNR, PSNR, and MSE metrics. Most notably PaLEnTIR reconstruction achieved a 0.85 SSIM whereas the L2-TV reconstruction scores only 0.52 as this metric is the most reflective of visual goodness and supports our visual critiques.

4.1.2. Salt and Pepper. The image corrupted by salt and pepper noise is shown in Figure 4.2.b. The data SNR of the input is 12.99dB. The L2-TV and the PaLEnTIR reconstructions of the image and the table of performance metrics are shown in Figure 4.4. By looking at Figure 4.4, we can observe that the PaLEnTIR managed to eliminate almost all the pixels flipped by the salt and pepper process and the reconstructed objects look homogeneous. On the other hand, the L2-TV approach passes a far larger number of the pixels flipped by the salt and pepper process compared to the PaLEnTIR reconstruction. Also the contrasts of the doughnut-shaped object and the outer square are less accurately recovered for the L2-TV case compared to PaLEnTIR. These differences are reflected in the performance table in Figure 4.4, where PaLEnTIR outperforms L2-TV reconstruction in all four cases. The MSE of the PaLEnTIR reconstruction is almost the half that of L2-TV while the PaLEnTIR SSIM is a factor 1.6 greater than L2-TV which suggests that the PaLEnTIR reconstruction is much better both in terms of visual goodness and absolute error. Both the PSNR and SNR values of PaLEnTIR reconstructions exceed L2-TV by more than 2dB.

4.1.3. Poisson. The Poisson input image is shown in Figure 4.2.c The data SNR of the input is 17.85dB. The L2-TV and the PaLEnTIR reconstructions of the image and the table of performance metrics are shown



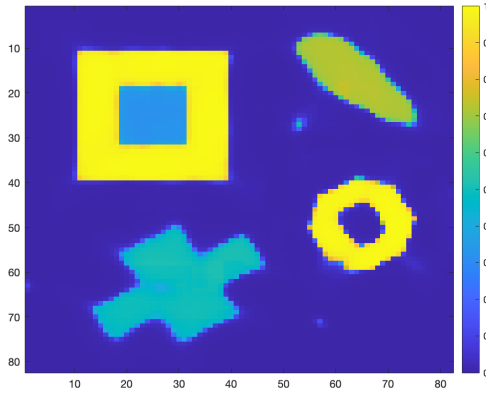
(a) PaLEnTIR reconstruction



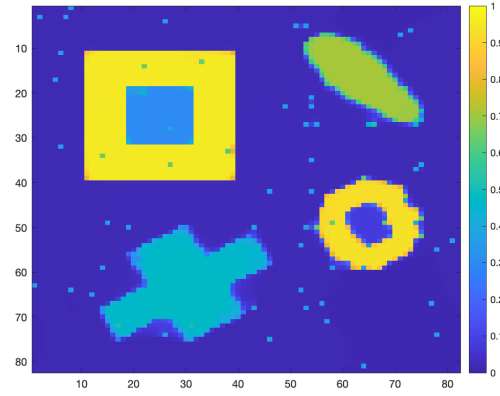
(b) TV reconstruction

Performance Metrics of the Denoising Experiment with Gaussian Noise					
Method	Number of Unknowns	PSNR	SNR	SSIM	MSE
Total Variation	6724	29.8906	22.2990	0.5203	0.0010
PaLEnTIR	432	30.9943	23.4026	0.8494	0.0008

Fig. 4.3: PaLEnTIR reconstruction and L2-TVreconstruction for the Gaussian denoising problem. The table shows the performance metrics for both methods. The better scores are written with bold letters.



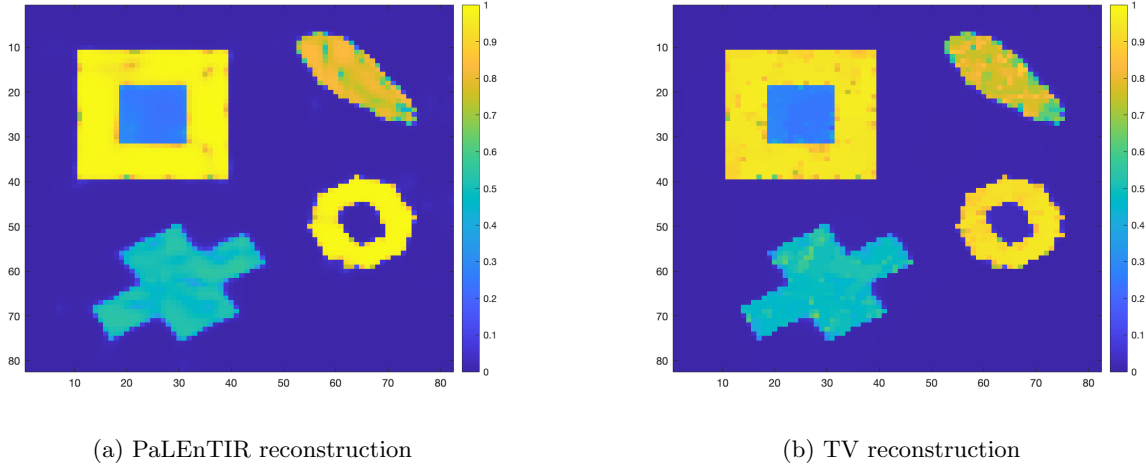
(a) PaLEnTIR reconstruction



(b) TV reconstruction

Performance Metrics of the Denoising Experiment with Salt and Pepper Noise					
Method	Number of Unknowns	PSNR	SNR	SSIM	MSE
Total Variation	6724	24.9233	17.3316	0.5383	0.0032
PaLEnTIR	432	27.4422	19.8506	0.9005	0.0018

Fig. 4.4: PaLEnTIR reconstruction and L2-TV reconstruction for the salt and pepper denoising problem. The table shows the performance metrics for both methods. The better scores are written with bold letters.



Performance Metrics of the Denoising Experiment with Poisson Noise					
Method	Number of Unknowns	PSNR	SNR	SSIM	MSE
Total Variation	6724	28.2279	20.6362	0.9263	0.0015
PaLenTIR	432	29.7828	22.1912	0.9471	0.0011

Fig. 4.5: PaLenTIR reconstruction and L2-TV reconstruction for the Poisson denoising problem. The table shows the performance metrics for both methods. The better scores are written with bold letters.

in Figure 4.5. The L2-TV reconstruction is strongly effected from the Poisson noise as it fails to recover the true contrast of the lower parts of the rotated ellipsoidal shape located at the upper right corner of the image. The artifacts on the objects reconstructed with the L2-TV approach are discrete and disturbing visually. Again PaLenTIR does well in terms of the four performance metrics.

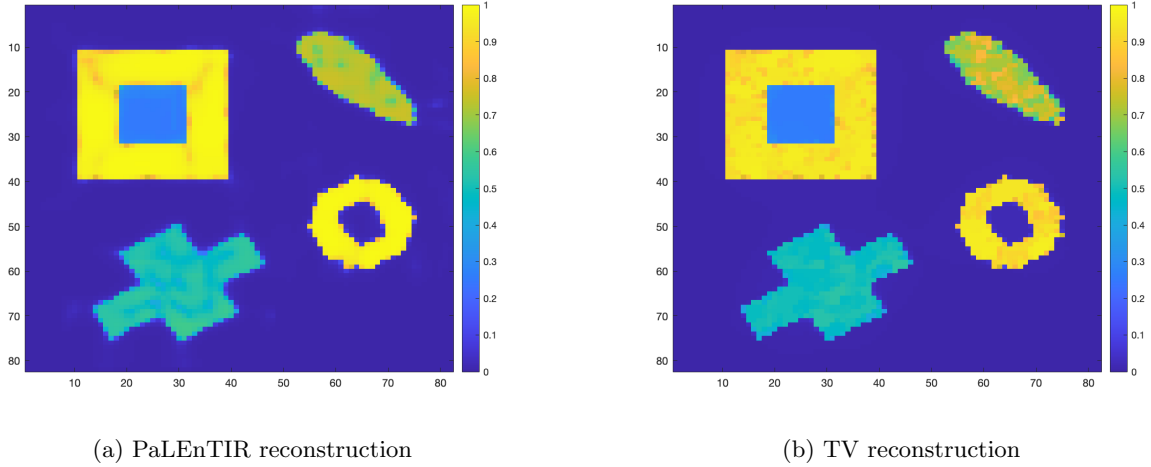
4.1.4. Speckle. The speckle input image is shown in Figure 4.2.d . The data SNR of the input is 19.40dB. The L2-TV and the PaLenTIR reconstructions of the image and the table of performance metrics are shown in Figure 4.6. The object on the top right corner looks very rough in the L2-TV reconstruction, the same issue can be observed with the both of the yellow objects. Except the object on the bottom left corner, other 3 objects look smoother in PaLenTIR reconstruction. Although PaLenTIR also has artifacts on the objects, these artifacts are fewer and smoother unlike the numerous small discrete artifacts on the L2-TV reconstruction which is visually disturbing. SSIM scores tell us that both reconstructions are visually good, L2-TV approach slightly outperforms. PaLenTIR reconstruction has slightly better PSNR and SNR values whereas both approach show comparable performance in terms of MSE.

4.2. Deconvolution. Deconvolution is a linear inverse problem where the desired signal must be recovered after it is convolved with a filter or a distortion function associated with an instrument or the physics of the problem [37, 61]. The discrete forward model for the deconvolution is defined via (3.1) as,

$$(4.4) \quad \mathbf{d} = \mathbf{A}\mathbf{f}(\mathbf{p}) + \mathbf{w},$$

where \mathbf{A} comes from discretizing an integral equation that represents convolution and \mathbf{w} is a vector of zero mean, independent Gaussian random variables.

In our deconvolution experiment, we seek to reconstruct the image in Figure 4.1 from the filtered and noise corrupted input data. The input data is formed by filtering the desired image with a 5×5 Gaussian kernel with a variance of 1 pixel. The data SNR of the input is 26.02dB. Figure 4.7 shows the L2-TV and PaLenTIR reconstructions as well as the table of performance metrics. The PaLenTIR reconstruction has reconstructed the edges of the shapes quite accurately and each region appears homogeneous. In contrast, the L2-TV reconstruction has a rough background, and the reconstructed objects have blurry edges. As a



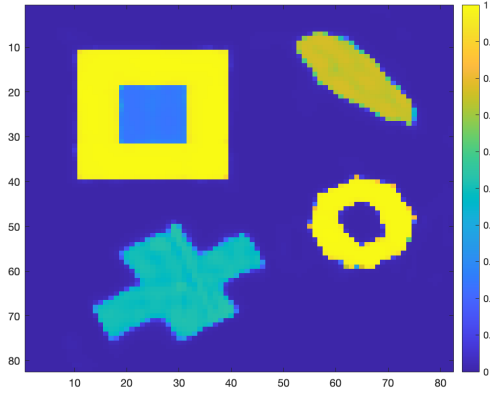
Performance Metrics of the Denoising Experiment with Speckle Noise					
Method	Number of Unknowns	PSNR	SNR	SSIM	MSE
Total Variation	6724	29.5582	21.9666	0.9595	0.0011
PaLenTIR	432	29.6340	22.0423	0.9384	0.0011

Fig. 4.6: The results of PaLenTIR reconstruction and L2-TV reconstruction for the speckle denoising problem. The table shows the performance metrics for both methods. The better scores are written with bold letters.

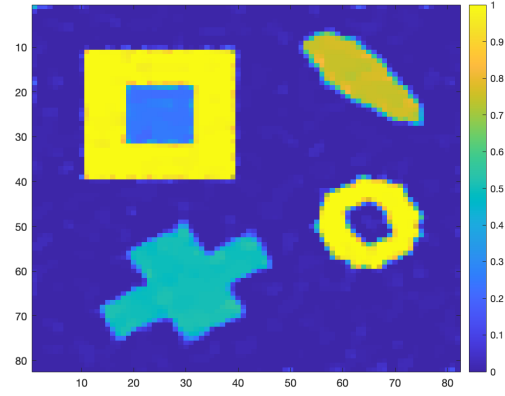
result, the MSE of the L2-TV reconstruction is more than three times that of the PaLenTIR reconstruction. The PaLenTIR reconstruction exceeds the L2-TV reconstruction by almost 5 dB in terms of both PSNR and SNR values. Also, the PaLenTIR reconstruction almost has a 0.97 SSIM value which cover 0.1 better than L2-TV.

4.3. X-ray Computed Tomography. X-ray computed tomography (CT) is typically well approximated as a linear problem and is one of the most common and well-known methods for medical imaging applications [19, 39]. As with deconvolution, the forward model takes the form of a matrix vector product, i.e. $\mathcal{M}(\mathbf{f}(\mathbf{p})) = \mathbf{R}\mathbf{f}(\mathbf{p})$ where \mathbf{R} denotes a (discrete) Radon transform, and the vector $\mathcal{M}(\mathbf{f}(\mathbf{p}))$ denotes the vectorized form of the sinogram data. In this paper, we explore the performance of PaLenTIR on both two and three dimensional forms of the CT problem focusing specifically on cases where there are a limited number of views.

4.3.1. 2D Tomography. For our 2D experiments, we use an open-access dataset of tomographic X-ray data of a carved cheese [13]. The image of the carved cheese as well as the ground truth reconstruction provided in the dataset is shown in Figure 4.8. We consider both sparse angle and limited angle problems. For the sparse angle case we take 15 projections spanning the full 360 degree circle whereas for the limited angle problem we use 15 projections spanning the range $1^\circ - 90^\circ$. In both experiments our PaLenTIR model consists of 144 basis functions. The total number of unknowns for the PaLenTIR model is 432. We compare the PaLenTIR reconstructions with both L2-TV reconstructions and Tikhonov reconstructions. The code for the Tikhonov method is given in [13]. For the TV method we used the code in the *TVReg* Matlab package for Total Variation Reconstruction [38]. For both of these reconstructions, the required number of unknowns is equal to $128 \times 128 = 16384$ which is almost 40 times more than the PaLenTIR model. Both the Tikhonov and L2-TV methods require their parameters to be selected. Unlike the other experiments, we could not directly select the best parameter for these methods. The reason is that the given ground truth data and the FBP data have a different scale/colorbar due to normalization. FBP is computed with an off-the-shelf FBP routine from Matlab and the value range is not compensated for. Instead, the iterative routine (which



(a) PaLEnTIR reconstruction



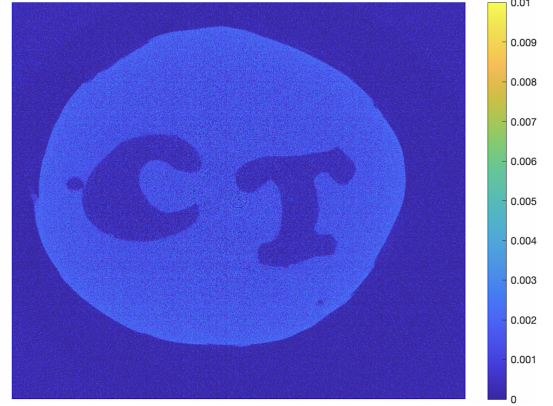
(b) TV reconstruction

Performance Metrics of the Deconvolution Experiment with Gaussian Noise					
Method	Number of Unknowns	PSNR	SNR	SSIM	MSE
Total Variation	6724	26.2987	18.7071	0.8615	0.0023
PaLEnTIR	432	31.2916	23.7000	0.9674	0.0007

Fig. 4.7: PaLEnTIR reconstruction and L2-TV reconstruction for the deconvolution problem. The table shows the performance metrics for both methods. The better scores are written with bold letters.



(a) The real image of the carved cheese



(b) Ground truth reconstruction of the cheese data

Fig. 4.8: The image of the carved cheese and the ground truth reconstruction of the cheese data provided in dataset [13]. The repository of the data can be found in [14]. The permission for displaying the real image of the carved cheese is granted by the author of the dataset.

use the explicit matrix) have normalized values. The parameter value for the Tikhonov method is given in [13]. For the L2-TV method we visually inspected the results for different parameters and picked the one that gives the highest quality reconstruction visually.

5. Sparse Angle Tomography. The three reconstructions for the sparse-angle problem are shown in Figure 5.1. All three methods are capable of recovering the general shape of the object. The Tikhonov reconstruction suffers from far more artifacts in the background than either L2-TV or PaLEnTIR. Moreover,

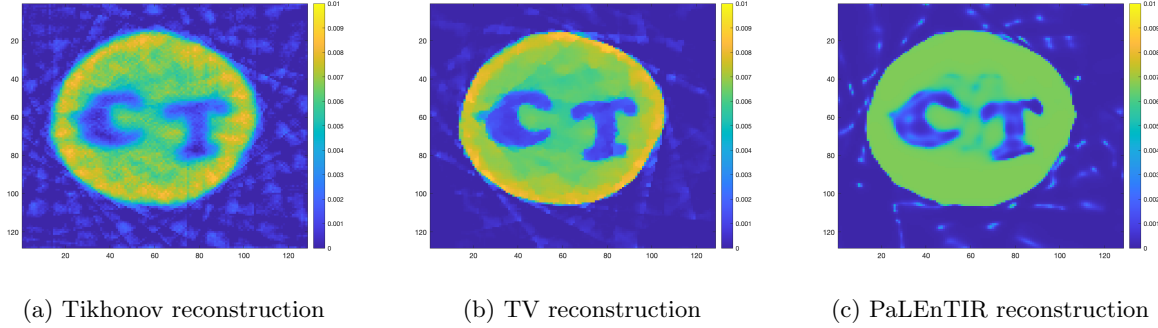


Fig. 5.1: Tikhonov, TV, and PaLenTIR reconstructions of the sparse angle tomography using the cheese data.

the small hole to the left of the “C” seen in Figure 4.8a, is recovered poorly in the Tikhonov case. The L2-TV reconstruction is much more successful in recovering the small hole and suppressing the background artifacts. The cheese has a smoother reconstruction in the L2-TV compared to the Tikhonov reconstruction. The PaLenTIR model with 144 basis functions has also managed to recover the object successfully. The inhomogeneities seen on the cheese surface in Tikhonov and l2-TV methods are rarely seen in PaLenTIR. The letters in PaLenTIR look more noisy than the L2-TV approach. However, L2-TV reconstruction misleads as if there is a contrast difference between the letters and the background. Both L2-TV and PaLenTIR reconstructions have background noise. L2-TV seems to have more artifacts at a lower contrast whereas PaLenTIR has fewer pixels that count as artifacts but they are much brighter. However, background is not our region of interest hence these artifacts are not a major concern. It is also possible to realize the small hole detail near the letter “C” from the PaLenTIR reconstruction which is very important considering the almost 38 folds more number of unknowns are required for the L2-TV and the Tikhonov reconstructions compared to the PaLenTIR.

Limited View Tomography. The three limited view reconstructions are shown in Figure 4.8. Here we see far more distortion, especially in the Tikhonov and L2-TV reconstruction than was the case with the sparse angle problem. In the Tikhonov case, it is almost impossible to locate the upper left and lower right parts of the object. The small hole near the letter “C” is completely missing. The L2-TV reconstruction is an improvement in that the upper left and lower right parts are better recovered although the boundary of the object is still blurry. The letters “C” and “T” are clearer compared to the Tikhonov case though they are still blurry. It is still not possible to observe the small hole in the L2-TV reconstruction. The PaLenTIR reconstruction eliminates the X-Ray artifacts in most of the image. The upper left and lower right portions (which the L2-TV and Tikhonov struggle to recover) as well as the letters are much clearer. Furthermore, the small hole that is completely lost in the other recoveries is clearly observable in the PaLenTIR reconstruction. There are few severe artifacts in the PaLenTIR reconstruction. Most of them are located in the background which is outside of our interest.

5.1. 3D Limited View Parallel Beam Tomography. We now explore the PaLenTIR model in the context of a 3D limited view parallel beam tomography experiment. For this experiment, we build the system matrix for the forward mapping in equation 4.2, using the TVReg Matlab package for Total Variation Reconstruction [38]. The desired 3D image is of size $27 \times 27 \times 27$ shown in Figure 5.3.a. The input data is formed from 31 projections where each projection has a projection plane center located on the surface of the quarter of a “lebedev sphere” [46] as shown in Figure 5.4. Additive Gaussian noise is added to the input data to achieve a noise level 1%. We used $7 \times 7 \times 7 = 343$ basis functions in the PaLenTIR model for this experiment. The reconstructed object is shown in Figure 5.3.b as well as the performance metrics of the PaLenTIR reconstruction. From Figure 5.3 and the PSNR value of the PaLenTIR reconstruction, we can conclude that the PaLenTIR model, with only 343 basis functions, succeeded in representing a 19683 pixel

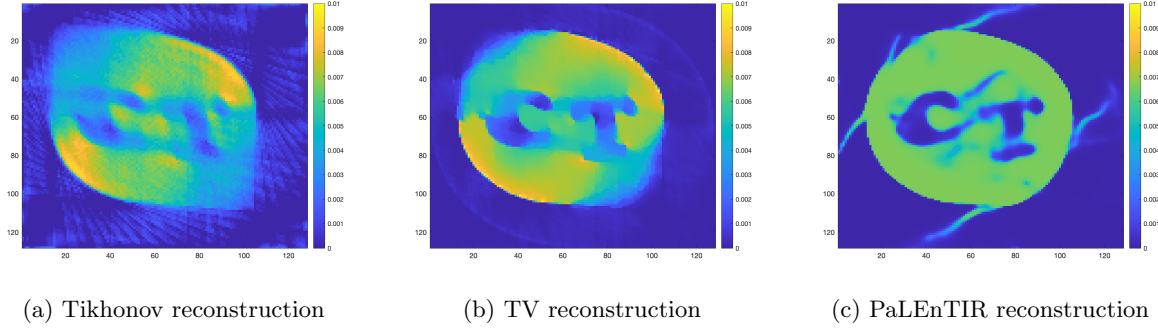
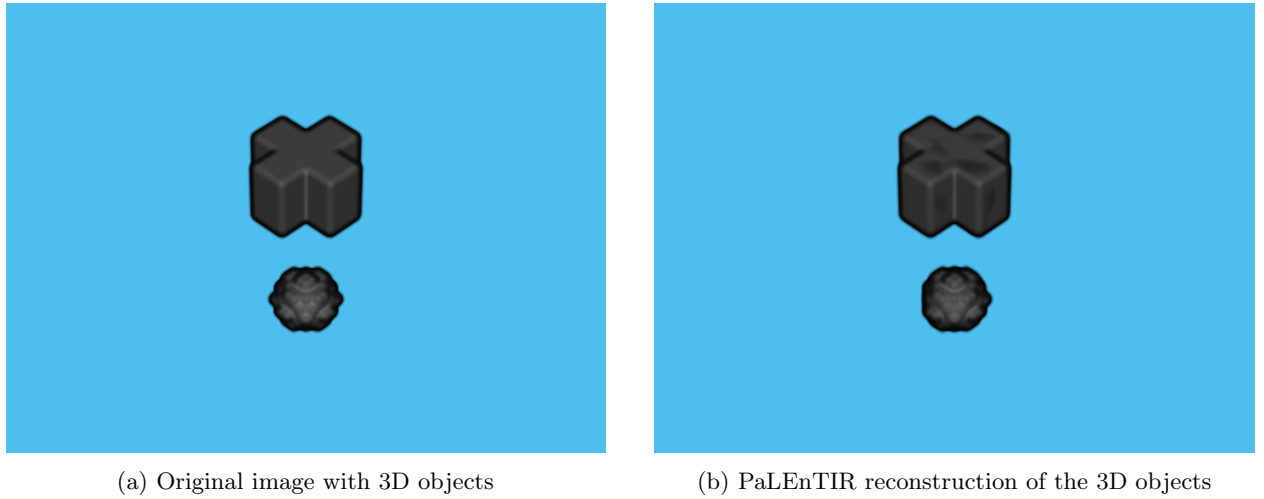


Fig. 5.2: Tikhonov, TV, and PaLEnTIR reconstructions of the limited angle tomography using the cheese data.



Performance Metrics of 3D Limited CT					
Method	Number of Unknowns	PSNR	SNR	SSIM	MSE
PaLEnTIR	343	35.1743	22.2507	0.9574	0.0003

Fig. 5.3: Results of 3D limited view parallel beam tomography experiment. a. original image of the 3D objects, b. PaLEnTIR reconstruction from the noisy limited CT data. The table shows the performance metrics of the PaLEnTIR reconstruction.

3D image with two 3D objects inside.

5.2. Diffuse Optical Tomography. Diffuse optical tomography (DOT) is a non-invasive, low-cost alternative for breast and brain imaging compared with X-ray and MRI [11]. In DOT, the tissue is illuminated with near infra-red light and the data, comprised of point measurements of diffused and partially absorbed photon fields, is collected external to the body. These measurements are used along with a mathematical model, typically a diffusion-absorption equation (posed in the frequency domain), to recover the optical absorption and (sometimes) scattering properties of the medium,

$$-\nabla \cdot (D(r)\nabla\eta(r)) + \mu(r;\mathbf{p})\eta(r) + \frac{i\omega}{\nu}\eta(r) = g(r),$$

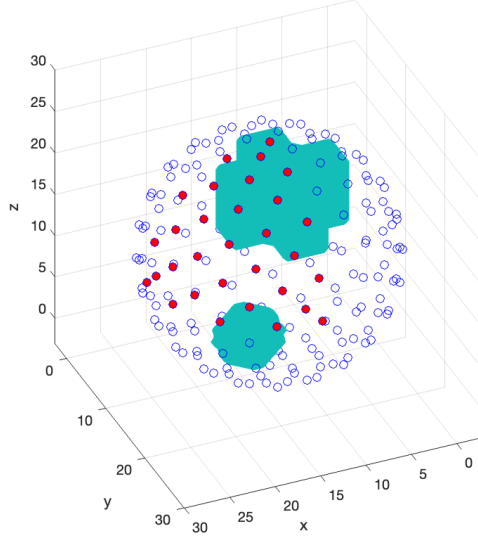


Fig. 5.4: Green objects represent the objects of interest in the 3D CT experiment. Blue points are the samples from a lebedev sphere surrounding the objects and centered at the origin. Red points are the chosen samples from the lebedev sphere to and are used as the projection plane centers in the 3D CT experiment. The projection plane centers are chosen such that they all are located at the same quarter of the lebedev sphere.

where $D(r)$ represents (here) the known scalar diffusion at a point r , $\mu(r; \mathbf{p})$ represents the absorption as a function of space and the parameter vector \mathbf{p} (that we are solving for), ω represents the modulation frequency of the light source, and ν represents the speed of light in the medium (tissue). The sources are placed one grid point inside the medium [5], and the detectors are placed on the opposite boundary. On the boundaries where the sources and detectors are located we have Robin boundary conditions; on the other boundaries we assume homogeneous Dirichlet boundary conditions, $\eta(r) = 0$. For details, see [6, 68]. The recovered absorption coefficient (and sometimes also the diffusion/scattering) can then be used to characterize the state of the tissue [11, 29, 30].

Following, e.g., [44], we assume that the absorption coefficient can be modeled via (3.1). As shown in Figure 5.5, we take the region to be imaged as a rectangle of size 4cm by 4cm, with $m_s = 32$ sources arrayed on the right side and $m_d = 32$ detectors on the left. As before, we let $\mathbf{f}(\mathbf{p})$ denote the discrete absorption image for a given parameter vector, that is, $[\mathbf{f}(\mathbf{p})]_i = f(\mathbf{r}_i, \mathbf{p})$ for any grid point \mathbf{r}_i . Assuming we collect data for all detectors when each source is active, we obtain a data vector \mathbf{d} with $m = m_s \times m_d$ values. The input-output map from sources to detectors (also called the *transfer function*) as a function of \mathbf{p} , is given by

$$(5.1) \quad \Psi(\mathbf{f}(\mathbf{p})) = \mathbf{C}^T \mathbf{A}(\mathbf{f}(\mathbf{p}))^{-1} \mathbf{B} \in \mathbb{R}^{m_d \times m_s},$$

where $\mathbf{B} \in \mathbb{R}^{n \times m_s}$ represents m_s sources, n is the total number of voxels or grid points, $\mathbf{A}(\mathbf{f}(\mathbf{p})) \in \mathbb{R}^{n \times n}$ represents the discretization of the diffusion-absorption equation, and $\mathbf{C}^T \in \mathbb{R}^{m_d \times n}$ simulates the measurement of outputs at m_d detectors. So, $\mathbf{A}(\mathbf{f}(\mathbf{p}))\mathbf{X} = \mathbf{B}$ represents the discretized PDE that relates photon fluence/flux at grid points to the sources [5]. The DOT inverse problem is then specified by the forward mapping $\mathcal{M}(\mathbf{f}(\mathbf{p})) = \text{vec}(\Psi(\mathbf{f}(\mathbf{p})))$, the vectorization of the transfer function output. Given a vector of measured data (with additive noise) \mathbf{d} , we solve for \mathbf{p} by minimizing $\frac{1}{2} \|\text{vec}(\Psi(\mathbf{f}(\mathbf{p}))) - \mathbf{d}\|_2^2$ (cf Algorithm 3.1). Note that regularization is provided implicitly by the parameterization.

We present results for a test case with the true anomaly as shown in Figure 5.5a. The focus of this test is the quality of the shape reconstruction using the new PaLEnTIR parameterization. We note that the

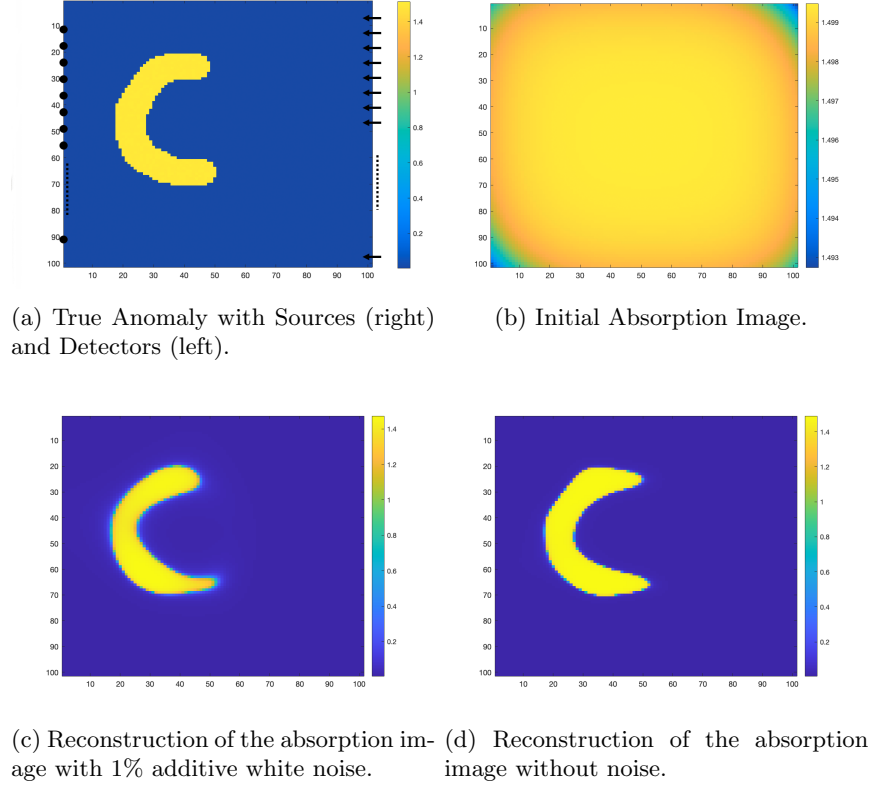


Fig. 5.5: Diffuse Optical Tomography experiment.

DOT problem is severely data limited, both due to limited numbers of sources and detectors as well as the highly diffuse nature of the problem, so accurate reconstructions are not possible. (This is why the shape-based parameterized reconstruction for problems with well-defined boundaries is important.) To distinguish between reconstruction error due to noise and ill-posedness and reconstruction error due to the nature of the problem, we provide a reconstruction with 1% noise (realistic) as well as one without noise. The latter serves to demonstrate the difficulty of the data limited problem which should be distinguished from the approximation quality of PaLEnTIR.

The initial absorption image (corresponding to initial parameter vector \mathbf{p}_0) is given in Figure 5.5b. The reconstruction for the data without noise is in the lower right of Figure 5.5. The model captures the structure quite well, with slight imperfections due to the data limited nature of the problem rather than the PaLEnTIR model. When noise is added and we run the algorithm we observe the image in the lower left. This is a remarkably good reconstruction given that there is noise in data, the forward model is nonlinear, and the measured data is limited. Moreover, it is important to note that there was no parameter to tune in generating this reconstruction.

6. Concluding Remarks. This paper considers a redefinition of the parametric level set method specifically intended to address issues arising in the context of ill-posed inverse problems. The main contribution of PaLEnTIR comes from replacing the binary Heaviside function used in the traditional PaLS models with a smooth transition function to allow for a single level set function to recover multiple disconnected objects with differing contrasts without needing to know the number of objects or the number and values of the contrasts. Current state-of-the-art formulations require either N or $\log_2 N$ level sets to recover a scene with piecewise constant objects possessing N unknown contrasts. As a result, current methods require prior knowledge of the number of contrasts. Our approach does require that we determine maps of both upper

and lower bounds of the contrast over a relatively coarse scale. For this, we proposed and experimentally explored a method iterates between estimation of the PaLEnTIR parameters and updating the bounds using min and max filters from the resulting image estimate.

The paper also showed through experiments that PaLEnTIR improves the shape-expressiveness of the PaLEnTIR compared to PaLS model with RBF formulation by allowing for non-isotropic basis functions that are capable of producing rotated ellipsoidal cross-sections. The new basis functions provide increased geometric flexibility and more easily capture complex details compared to RBF formulation which only used circular shapes to construct objects. We provided our parameterization of the Stretch and Slide matrix for both the 2D and the 3D PaLEnTIR model. For the 2D Stretch and Slide matrix, instead of parameterizing all 4 elements of the matrix or using 3 parameter parametrization of the Cholesky factorization of the symmetric matrix, we proposed a 2-parameter factorization. The "stretching" and "sliding" operations on the ellipse combined with the expansion by the weight coefficient give the enough degree of freedom to basis functions. We also underlined the similar results and inferences for the 3D dilation matrix.

Furthermore, we discuss that PaLEnTIR is superior in terms of it's numerical performance compared to PaLS with RBF formulation, which is empirically shown in this paper with the condition number plots of the models for both single and multiple basis functions formulations. The numerical improvements of PaLEnTIR are connected to the improvements in the following issues; Total number of parameters, Sensitivity to parameters, Non-uniqueness of parametric to image mappings. Total number of parameters are significantly reduced in PaLEnTIR due to various reasons mentioned in this paper. First of all, the sufficiency of a single level set function to solve a multi-contrast problem reduces the number of parameters to "*one N'th*" of what most of the current state-of-the-art methods require. Secondly, the flexibility of shape representation in the new anisotropic basis functions can represent the shapes with fewer basis functions compared to the previous RBFs which means less basis functions and consequently less parameters. The choice of Stretch and Slide matrix, a 2 parameter factorization of the SPD matrix, further reduces the number of parameters compared to the parametrization of all 4 elements of a general 2D matrix for dilation and rotation operations (similar improvements in 3D as well). Finally, the fixed centers of basis functions also reduce the number of parameters by 2 (3 for 3D) per basis function. All the above-mentioned reductions result in a significant decrease in number of parameters. Besides that, the use of the hyperbolic tangent function in the definition of the weight parameters and fixed centers of basis functions prevent the domination of few basis functions in the entire reconstruction. On the contrary, these changes encourage each basis function to contribute in the reconstruction. As a result, the sensitivity to parameters of the PaLS model improves in PaLEnTIR. Finally, by leaving the expansion of the ellipses solely on the expansion coefficient (similarly the stretching for β and sliding for γ), we minimize the non-uniqueness of parametric to image mappings. Specifically, our model avoids having the same shape representation of a basis function either by suitable changes to dilation or suitable changes to the amplitude, as it is the case for the RBFs. Furthermore, fixing the centers of basis functions make the reconstructions sensitive to the permutations of the basis functions, i.e. we could have the same reconstruction by swapping the parameters of 2 different RBFs in case of parameterized center locations, which is against to the uniqueness of of parametric to image mappings.

To explore the utility of PaLEnTIR, we considered numerical experiments over a wide range of inverse problems. For 2D denoising, deconvolution, and X-ray Computed Tomography, we compared our method to pixel-based methods where it generally provided performance better than that of Tikhonov and total variation based methods where, importantly, we chose the regularization parameters to minimize the true mean square error, an option obviously not available in practice. For denoising, we demonstrated the ability of our model to provide strong results for data corrupted by or reflecting a broad assortment of practically interesting sources of randomness. All of these problems have different "optimal" estimation formulations which, except for the Gaussian case, do not result in least squares problems. We note that PaLEnTIR shows uniformly strong performance in terms of both mathematically and visually (PSNR > 27dB, SSIM > 0.84) using a common least square error criterion and without the need for any parameter tuning on all of these very different cases. We also examined a severely limited view 3D parallel beam tomography problem where PaLEnTIR successfully recovered two volumetric objects despite the limited data and presence of additive Gaussian noise. To show that PaLEnTIR is not limited to linear inverse problems, we used the proposed method on a Diffuse Optical Tomography problem, a very ill-posed non-linear inverse problem. PaLEnTIR succeeded in capturing the edge and shape information of the object with a very few number of

basis functions relative to number of unknowns in pixel-based methods.

The strong performance of PaLEnTIR motivates a number of areas where future efforts are needed. Although the results of our numerical experiments are promising, a more thorough exploration of 3D and nonlinear problems is needed. We plan to delve more into 3D problems and test the model with several different 3D, nonlinear ill-posed problems. While PaLEnTIR worked well using homogeneously distributed basis functions, we believe that the performance of the model can be further improved through the use of some type of adaptive refinement strategy similar to [7, 8] which places more basis functions in regions where there is, in some sense, greater geometric detail. Of great interest to us is better understanding the convergence properties of the iteration used to determine C_L and C_H . To supplement the strong numerical results, we believe it should be possible to better understand the behavior of this method at least in the context of simple “toy” problems such as the recovery of a 1D step discontinuity. Finally, we will investigate the use of this model for Uncertainty Quantification focusing on building prior models for the PaLEnTIR parameters from priors on the objects for which we are looking as well as the use of these priors for quantifying e.g., accuracy in localizing and characterizing objects to be recovered.

References.

- [1] R. Acar and C. Vogel. “Analysis of bounded variation penalty methods for ill-posed problems”. In: *Inverse Problems* 10 (1994), pp. 1217–1229.
- [2] Alireza Aghasi, Misha Kilmer, and Eric Miller. “Parametric Level Set Methods for Inverse Problems”. In: *SIAM J. Imaging Sciences* 4 (July 2011). DOI: [10.1137/100800208](https://doi.org/10.1137/100800208).
- [3] Alireza Aghasi et al. “A geometric approach to joint inversion with applications to contaminant source zone characterization”. In: *Inverse problems* 29.11 (2013), p. 115014.
- [4] G. Allaire et al. “Multi-phase structural optimization via a level set method”. In: *ESAIM: Control, Optimisation and Calculus of Variations* 20.2 (2014), pp. 576–611. DOI: [10.1051/cocv/2013076](https://doi.org/10.1051/cocv/2013076).
- [5] S. R. Arridge. “Optical tomography in medical imaging”. In: *Inverse Problems* Vol. 16 (1999), R41–R93.
- [6] Selin S. Aslan, Eric de Sturler, and Misha E. Kilmer. “Randomized approach to nonlinear inversion combining random and optimized simultaneous sources and detectors”. In: *SIAM J. Sci. Comput* 41 (2019), B229–B249.
- [7] Alexandre Baussard, Eric L Miller, and Dominique Lesselier. “Adaptive multiscale reconstruction of buried objects”. In: *Inverse Problems* 20.6 (2004), S1.
- [8] Alexandre Baussard, Eric L Miller, and Denis Prémel. “Adaptive B-spline scheme for solving an inverse scattering problem”. In: *Inverse Problems* 20.2 (2004), p. 347.
- [9] M Ben, Mohamed Khames Ben Hadj Miled, and Eric Miller. “A projection-based level-set approach to enhance conductivity anomaly reconstruction in electrical resistance tomography”. In: *Inverse Problems* 23 (Dec. 2007), pp. 2375–2400. DOI: [10.1088/0266-5611/23/6/007](https://doi.org/10.1088/0266-5611/23/6/007).
- [10] D.P. Bertsekas and W. Rheinboldt. *Constrained Optimization and Lagrange Multiplier Methods*. Computer science and applied mathematics. Elsevier Science, 2014. ISBN: 9781483260471. URL: <https://books.google.com/books?id=j6LiBQAAQBAJ>.
- [11] DA Boas et al. “Imaging the body with diffuse optical tomography”. In: *IEEE Signal Processing Magazine* 18.6 (2001), pp. 57–75.
- [12] T. Brox and J. Weickert. “Level Set Segmentation With Multiple Regions”. In: *IEEE Transactions on Image Processing* 15.10 (2006), pp. 3213–3218. DOI: [10.1109/TIP.2006.877481](https://doi.org/10.1109/TIP.2006.877481).
- [13] Tatiana A. Bubba et al. *Tomographic X-ray data of carved cheese*. 2017. arXiv: [1705.05732](https://arxiv.org/abs/1705.05732) [physics.med-ph].
- [14] Tatiana A. Bubba et al. *Tomographic X-ray data of carved cheese*. Version 1.0.0. Zenodo, May 2017. DOI: [10.5281/zenodo.1254210](https://doi.org/10.5281/zenodo.1254210). URL: <https://doi.org/10.5281/zenodo.1254210>.
- [15] Stanley Chan. *deconvtv - fast algorithm for total variation deconvolution*. MATLAB Central File Exchange. 2022.
- [16] Tony Chan and Luminita Vese. “Active Contours without Edges”. In: *IEEE Transactions on Image Processing* 10 (Jan. 2001), pp. 266–277.

- [17] Chi-Chih Chen et al. “Ultrawide-bandwidth fully-polarimetric ground penetrating radar classification of subsurface unexploded ordnance”. In: *IEEE Transactions on Geoscience and Remote Sensing* 39.6 (2001), pp. 1221–1230.
- [18] W Dailey and A Ramirez. “Electrical impedance tomography of the 1995 OGI perchloroethylene release”. In: (Oct. 1996). DOI: [10.2172/461374](https://doi.org/10.2172/461374). URL: <https://www.osti.gov/biblio/461374>.
- [19] Mark E. Davison. “The Ill-Conditioned Nature of the Limited Angle Tomography Problem”. In: *SIAM Journal on Applied Mathematics* 43.2 (1983), pp. 428–448. DOI: [10.1137/0143028](https://doi.org/10.1137/0143028). eprint: <https://doi.org/10.1137/0143028>. URL: <https://doi.org/10.1137/0143028>.
- [20] Ross W Deming and Anthony J Devaney. “Diffraction tomography for multi-monostatic ground penetrating radar imaging”. In: *Inverse Problems* 13.1 (1997), p. 29.
- [21] Zhiliang Deng, Xiaomei Yang, and Jiangfeng Huang. *A parametric Bayesian level set approach for acoustic source identification using multiple frequency information*. 2019. arXiv: [1907.08660](https://arxiv.org/abs/1907.08660) [math.NA].
- [22] J. E. Dennis and Robert B. Schnabel. *Numerical Methods for Unconstrained Optimization and Nonlinear Equations*. Society for Industrial and Applied Mathematics, 1996. DOI: [10.1137/1.9781611971200](https://doi.org/10.1137/1.9781611971200). eprint: <https://epubs.siam.org/doi/pdf/10.1137/1.9781611971200>. URL: <https://epubs.siam.org/doi/abs/10.1137/1.9781611971200>.
- [23] Kees van den Doel and U. Ascher. “On level set regularization for highly ill-posed distributed parameter estimation problems”. In: *Journal of Computational Physics* 216 (Aug. 2006), pp. 707–723. DOI: [10.1016/j.jcp.2006.01.022](https://doi.org/10.1016/j.jcp.2006.01.022).
- [24] Oliver Dorn and Dominique Lesselier. “Level set methods for inverse scattering”. In: *Inverse Problems* 22 (June 2006), R67. DOI: [10.1088/0266-5611/22/4/R01](https://doi.org/10.1088/0266-5611/22/4/R01).
- [25] Oliver Dorn and Dominique Lesselier. “Level set techniques for structural inversion in medical imaging”. In: *Deformable Models*. Springer, 2007, pp. 61–90.
- [26] Moshe Eliasof, Andrei Sharf, and Eran Treister. “Multi-modal 3D Shape Reconstruction Under Calibration Uncertainty using Parametric Level Set Methods”. In: *CoRR* abs/1904.10379 (2019). arXiv: [1904.10379](https://arxiv.org/abs/1904.10379). URL: <http://arxiv.org/abs/1904.10379>.
- [27] H.W. Engl, M. Hanke, and A. Neubauer. *Regularization of Inverse Problems*. Mathematics and Its Applications. Springer Netherlands, 1996. ISBN: 9780792341574. URL: <https://books.google.com/books?id=2bzgmMv5EVcC>.
- [28] Sarah Fakhreddine et al. “Imaging geochemical heterogeneities using inverse reactive transport modeling: An example relevant for characterizing arsenic mobilization and distribution”. In: *Advances in Water Resources* 88 (2016), pp. 186–197.
- [29] Qianqian Fang et al. “Combined optical and X-ray tomosynthesis breast imaging 1”. In: *Radiology* 258.1 (2011), pp. 89–97.
- [30] Qianqian Fang et al. “Combined optical imaging and mammography of the healthy breast: optical contrast derived from breast structure and compression”. In: *Medical Imaging, IEEE Transactions on* 28.1 (2009), pp. 30–42.
- [31] Haihua Feng, W.C. Karl, and D.A. Castanon. “A curve evolution approach to object-based tomographic reconstruction”. In: *IEEE Transactions on Image Processing* 12.1 (2003), pp. 44–57. DOI: [10.1109/TIP.2002.806253](https://doi.org/10.1109/TIP.2002.806253).
- [32] S. J. Hamilton and A. Hauptmann. “Deep D-Bar: Real-Time Electrical Impedance Tomography Imaging With Deep Neural Networks”. In: *IEEE Transactions on Medical Imaging* 37.10 (2018), pp. 2367–2377. DOI: [10.1109/TMI.2018.2828303](https://doi.org/10.1109/TMI.2018.2828303).
- [33] A. J. Hiles and O. Dorn. “Colour level set regularization for the electromagnetic imaging of highly discontinuous parameters in 3D”. In: *Inverse Problems in Science and Engineering* 29.4 (2021), pp. 489–524. DOI: [10.1080/17415977.2020.1797003](https://doi.org/10.1080/17415977.2020.1797003). eprint: <https://doi.org/10.1080/17415977.2020.1797003>. URL: <https://doi.org/10.1080/17415977.2020.1797003>.
- [34] G. Hoversten et al. “Borehole to Surface Electromagnetic Monitoring of Hydraulic Fractures”. In: June 2017. DOI: [10.3997/2214-4609.201700853](https://doi.org/10.3997/2214-4609.201700853).
- [35] G. Hoversten et al. “Multi-physics Inversion for Reservoir Monitoring”. In: May 2016. DOI: [10.3997/2214-4609.201601658](https://doi.org/10.3997/2214-4609.201601658).

- [36] Gabriele Incorvaia and Oliver Dorn. “Stochastic Optimization Methods for Parametric Level Set Reconstructions in 2D through-the-Wall Radar Imaging”. In: *Electronics* 9.12 (2020). ISSN: 2079-9292. DOI: [10.3390/electronics9122055](https://doi.org/10.3390/electronics9122055). URL: <https://www.mdpi.com/2079-9292/9/12/2055>.
- [37] Peter A. Jansson. “Deconvolution of images and spectra”. In: 1997.
- [38] Tobias Lindstrøm Jensen et al. *TVReg*. English. 2010.
- [39] Willi Kalender. “X-ray computed tomography”. In: *Physics in medicine and biology* 51 (Aug. 2006), R29–43. DOI: [10.1088/0031-9155/51/13/R03](https://doi.org/10.1088/0031-9155/51/13/R03).
- [40] Misha Kilmer et al. “Cortical constraint method for diffuse optical brain imaging”. In: *Advanced Signal Processing Algorithms, Architectures, and Implementations XIV*. Ed. by Franklin T. Luk. Vol. 5559. International Society for Optics and Photonics. SPIE, 2004, pp. 381–391. URL: <https://doi.org/10.1117/12.559745>.
- [41] Andreas Kirsch. “Characterization of the shape of a scattering obstacle using the spectral data of the far field operator”. In: *Inverse Problems* 14 (1998), pp. 1489–1512.
- [42] Ville Kolehmainen, Matti Lassas, and Samuli Siltanen. “Limited Data X-Ray Tomography Using Non-linear Evolution Equations”. In: *SIAM J. Scientific Computing* 30 (Jan. 2008), pp. 1413–1429. DOI: [10.1137/050622791](https://doi.org/10.1137/050622791).
- [43] R Kress and W Rundell. “A quasi-Newton method in inverse obstacle scattering”. In: *Inverse Problems* 10.5 (Oct. 1994), pp. 1145–1157. DOI: [10.1088/0266-5611/10/5/011](https://doi.org/10.1088/0266-5611/10/5/011). URL: <https://doi.org/10.1088/0266-5611/10/5/011>.
- [44] Fridrik Larusson, Sergio Fantini, and Eric L Miller. “Parametric level set reconstruction methods for hyperspectral diffuse optical tomography”. In: *Biomedical optics express* 3.5 (2012), pp. 1006–1024.
- [45] Fridrik Larusson et al. “Parametric estimation of 3D tubular structures for diffuse optical tomography”. In: *Biomedical optics express* 4 (Feb. 2013), pp. 271–86. DOI: [10.1364/BOE.4.000271](https://doi.org/10.1364/BOE.4.000271).
- [46] Vyacheslav Ivanovich Lebedev. “Quadratures on a sphere”. In: *USSR Computational Mathematics and Mathematical Physics* 16.2 (1976), pp. 10–24.
- [47] R. Li et al. “An Image Reconstruction For Electrical Capacitance Tomography Using Parametric Level Set”. In: *2020 5th International Conference on Computer and Communication Systems (ICCCS)*. 2020, pp. 384–390. DOI: [10.1109/ICCCS49078.2020.9118589](https://doi.org/10.1109/ICCCS49078.2020.9118589).
- [48] J. Lie, M. Lysaker, and Xue-Cheng Tai. “A binary level set model and some applications to Mumford-Shah image segmentation”. In: *IEEE Transactions on Image Processing* 15.5 (2006), pp. 1171–1181. DOI: [10.1109/TIP.2005.863956](https://doi.org/10.1109/TIP.2005.863956).
- [49] D. Liu, D. Smyl, and J. Du. “Nonstationary Shape Estimation in Electrical Impedance Tomography Using a Parametric Level Set-Based Extended Kalman Filter Approach”. In: *IEEE Transactions on Instrumentation and Measurement* 69.5 (2020), pp. 1894–1907. DOI: [10.1109/TIM.2019.2921441](https://doi.org/10.1109/TIM.2019.2921441).
- [50] Dong Liu, Danny Smyl, and Jiangfeng Du. “Comparison of different radial basis functions for parametric level set based method in electrical impedance tomography”. In: Sept. 2018.
- [51] Jikai Liu and Yongsheng Ma. “A new multi-material level set topology optimization method with the length scale control capability”. In: *Computer Methods in Applied Mechanics and Engineering* 329 (2018), pp. 444–463. ISSN: 0045-7825. DOI: <https://doi.org/10.1016/j.cma.2017.10.011>. URL: <https://www.sciencedirect.com/science/article/pii/S0045782517306795>.
- [52] M.S. McMillan et al. “3D Multiple Body Parametric Inversion of Time-domain Airborne EM Data”. In: 2015.1 (2015), pp. 1–5. ISSN: 2214-4609. DOI: <https://doi.org/10.3997/2214-4609.201413870>. URL: <https://www.earthdoc.org/content/papers/10.3997/2214-4609.201413870>.
- [53] Michael Mcmillan et al. “Multiple body parametric inversion of frequency- and time-domain airborne electromagnetics”. In: Sept. 2016, pp. 846–851. DOI: [10.1190/segam2016-13868448.1](https://doi.org/10.1190/segam2016-13868448.1).
- [54] F. Mesadi, M. Cetin, and T. Tasdizen. “Disjunctive normal level set: An efficient parametric implicit method”. In: *2016 IEEE International Conference on Image Processing (ICIP)*. 2016, pp. 4299–4303. DOI: [10.1109/ICIP.2016.7533171](https://doi.org/10.1109/ICIP.2016.7533171).
- [55] Eric L Miller, Misha Kilmer, and Carey Rappaport. “A new shape-based method for object localization and characterization from scattered field data”. In: *IEEE Transactions on Geoscience and Remote Sensing* 38.4 (2000), pp. 1682–1696.

- [56] Naren Naik, Rick Beatson, and Jerry Eriksson. “Radial-basis-function level-set-based regularized Gauss–Newton-filter reconstruction scheme for dynamic shape tomography”. In: *Applied Optics* 53 (Oct. 2014). DOI: [10.1364/AO.53.006872](https://doi.org/10.1364/AO.53.006872).
- [57] Stanley Osher and James A Sethian. “Fronts propagating with curvature-dependent speed: Algorithms based on Hamilton-Jacobi formulations”. In: *Journal of Computational Physics* 79.1 (1988), pp. 12–49. ISSN: 0021-9991. DOI: [https://doi.org/10.1016/0021-9991\(88\)90002-2](https://doi.org/10.1016/0021-9991(88)90002-2). URL: <https://www.sciencedirect.com/science/article/pii/0021999188900022>.
- [58] Stanley J. Osher and Fadil Santosa. “Level Set Methods for Optimization Problems Involving Geometry and Constraints: I. Frequencies of a Two-Density Inhomogeneous Drum”. In: *Journal of Computational Physics* 171.1 (2001), pp. 272–288. ISSN: 0021-9991. DOI: <https://doi.org/10.1006/jcph.2001.6789>. URL: <https://www.sciencedirect.com/science/article/pii/S0021999101967890>.
- [59] Gad El-Qady et al. “Imaging subsurface cavities using geoelectric tomography and ground-penetrating radar”. In: *Journal of cave and karst studies* 67.3 (2005), pp. 174–181.
- [60] I.T. Rekanos, T.V. Yioultsis, and T.D. Tsiboukis. “Inverse scattering using the finite-element method and a nonlinear optimization technique”. In: *IEEE Transactions on Microwave Theory and Techniques* 47.3 (1999), pp. 336–344. DOI: [10.1109/22.750236](https://doi.org/10.1109/22.750236).
- [61] S.M. Riad. “The deconvolution problem: An overview”. In: *Proceedings of the IEEE* 74.1 (1986), pp. 82–85. DOI: [10.1109/PROC.1986.13407](https://doi.org/10.1109/PROC.1986.13407).
- [62] Christophe Samson et al. “A Level Set Model for Image Classification”. In: *International Journal of Computer Vision* 40 (Jan. 2000), pp. 187–197. DOI: [10.1023/A:1008183109594](https://doi.org/10.1023/A:1008183109594).
- [63] Fadil Santosa. “A level-set approach for inverse problems involving obstacles Fadil SANTOSA”. In: *ESAIM: Control, Optimisation and Calculus of Variations* 1 (1996), pp. 17–33. DOI: [10.1051/cocv:1996101](https://doi.org/10.1051/cocv:1996101).
- [64] O. Semerci and E. L. Miller. “A Parametric Level-Set Approach to Simultaneous Object Identification and Background Reconstruction for Dual-Energy Computed Tomography”. In: *IEEE Transactions on Image Processing* 21.5 (2012), pp. 2719–2734. DOI: [10.1109/TIP.2012.2186308](https://doi.org/10.1109/TIP.2012.2186308).
- [65] David F. Shanno. “Conditioning of Quasi-Newton Methods for Function Minimization”. In: *Mathematics of Computation* 24 (1970), pp. 647–656.
- [66] Yanyan Shi et al. “A Non-Convex L1-Norm Penalty-Based Total Generalized Variation Model for Reconstruction of Conductivity Distribution”. In: *IEEE Sensors Journal* 20.14 (2020), pp. 8137–8146. DOI: [10.1109/JSEN.2020.2981873](https://doi.org/10.1109/JSEN.2020.2981873).
- [67] Eric de Sturler and Misha Kilmer. “A Regularized Gauss–Newton Trust Region Approach to Imaging in Diffuse Optical Tomography”. In: *SIAM J. Scientific Computing* 33 (Jan. 2011), pp. 3057–3086. DOI: [10.1137/100798181](https://doi.org/10.1137/100798181).
- [68] Eric de Sturler et al. “Nonlinear Parametric Inversion Using Interpolatory Model Reduction”. In: *SIAM J. Sci. Comput* 37(3) (2015), B495–B517.
- [69] Xue-Cheng Tai and TONY CHAN. “A survey on multiple level set methods with applications for identifying piecewise constant functions”. In: *International Journal of Numerical Analysis and Modeling* 1 (Jan. 2004).
- [70] Andrey N. Tikhonov and Vasiliy Y. Arsenin. *Solutions of ill-posed problems*. Translated from the Russian, Preface by translation editor Fritz John, Scripta Series in Mathematics. Washington, D.C.: John Wiley & Sons, New York: V. H. Winston & Sons, 1977, pp. xiii+258.
- [71] Bruce J Tromberg et al. “Assessing the future of diffuse optical imaging technologies for breast cancer management”. In: *Medical physics* 35.6Part1 (2008), pp. 2443–2451.
- [72] Andy Tsai, A. Jr, and A.S. Willsky. “Curve evolution implementation of the Mumford-Shah functional for image segmentation, denoising, interpolation, and magnification”. In: *Image Processing, IEEE Transactions on* 10 (Sept. 2001), pp. 1169–1186. DOI: [10.1109/83.935033](https://doi.org/10.1109/83.935033).
- [73] L. Vese and T. Chan. “A Multiphase Level Set Framework for Image Segmentation Using the Mumford and Shah Model”. In: *International Journal of Computer Vision* 50 (2004), pp. 271–293.
- [74] Rossmary Villegas et al. “Simultaneous Characterization of Geological Shapes and Permeability Distributions in Reservoirs Using the Level Set Method”. In: June 2006. DOI: [10.2523/100291-MS](https://doi.org/10.2523/100291-MS).

- [75] Curtis R. Vogel. *Computational Methods for Inverse Problems*. Society for Industrial and Applied Mathematics, 2002. DOI: [10.1137/1.9780898717570](https://doi.org/10.1137/1.9780898717570). eprint: <https://epubs.siam.org/doi/pdf/10.1137/1.9780898717570>. URL: <https://epubs.siam.org/doi/abs/10.1137/1.9780898717570>.
- [76] Michael Yu Wang and Xiaoming Wang. ““Color” level sets: a multi-phase method for structural topology optimization with multiple materials”. In: *Computer Methods in Applied Mechanics and Engineering* 193.6 (2004), pp. 469–496. ISSN: 0045-7825. DOI: <https://doi.org/10.1016/j.cma.2003.10.008>. URL: <https://www.sciencedirect.com/science/article/pii/S0045782503005644>.
- [77] Zhou Wang et al. “Image quality assessment: from error visibility to structural similarity”. In: *IEEE Transactions on Image Processing* 13.4 (2004), pp. 600–612. DOI: [10.1109/TIP.2003.819861](https://doi.org/10.1109/TIP.2003.819861).
- [78] Charles J Werth et al. “A review of non-invasive imaging methods and applications in contaminant hydrogeology research”. In: *Journal of contaminant hydrology* 113.1-4 (2010), pp. 1–24.
- [79] Quan Zhang et al. “Coregistered tomographic x-ray and optical breast imaging: initial results”. In: *Journal of biomedical optics* 10.2 (2005), p. 024033.
- [80] Hong-Kai Zhao et al. “A Variational Level Set Approach to Multiphase Motion”. In: *Journal of Computational Physics* 127.1 (1996), pp. 179–195. ISSN: 0021-9991. DOI: <https://doi.org/10.1006/jcph.1996.0167>. URL: <https://www.sciencedirect.com/science/article/pii/S0021999196901679>.

Appendix A. Parameter selection and initialization. In the experiments, N^2 basis functions are centered on an equally spaced $N \times N$ grid. The weight parameters α_i of basis functions are sampled from a zero-mean uniform distribution with a standard deviation of 0.01, $U(-0.02, 0.02)$. The dilation parameters β_i are all initialized to 0.015 and the rotation parameters γ_i are all initialized to 0.1. The space varying contrast limits are all initialized to the maximum (for C_H) and minimum (for C_L) values of the overall image while using the algorithm (3.1). The window size of max/min windows for the algorithm (3.1) is chosen as 29x29. For linear problems, the fixed constant μ in matrices \mathbf{R} and \mathbf{R}_3 in (3.5) and (3.11) are chosen as 10, in DOT problem it is chosen as 1 because of different grid spacing. The steepness coefficient w of the transition function in (3.3) is chosen as 0.05 for 2D problems and 0.001 for the 3D problem since it is a binary contrast problem. The c -level is chosen as 0.01.

Appendix B. TREGS Settings. In this section we give details about how we used TREGS algorithm in our experiments. For more specific details about the algorithm please refer to [67]. We give the initial parameter vector as specified in section A. The algorithm requires the Jacobian matrix as well. The derivatives for Jacobian calculation are given in the following sections. We used 3 stopping criteria for our experiments. The first criterion is the drop of the residual decrease between two consecutive TREGS iterations below 0.001. The second stopping criterion is the drop of the residual to the level of the noise norm of the input data. The final criterion is reaching the maximum iteration number which we chose as 10000.

Appendix C. Derivatives of the PaLS with respect to model parameters. In this section we show the derivatives of the PaLS in (2.6). The PaLS model is defined as,

$$(C.1) \quad f(\mathbf{r}; \mathbf{p}) = C_H(\mathbf{r})H_\epsilon(\phi_{og}(\mathbf{r}; \mathbf{p})) + C_L(\mathbf{r})(1 - H_\epsilon(\phi_{og}(\mathbf{r}; \mathbf{p})))$$

The derivative of $f(\mathbf{r}; \mathbf{p})$ with respect to a parameter p_i is written by using the chain rule as,

$$(C.2) \quad \frac{\partial f(\mathbf{r}; \mathbf{p})}{\partial p_j} = (C_H(\mathbf{r}) - C_L(\mathbf{r})) \frac{\partial H_\epsilon(\phi_{og}(\mathbf{r}; \mathbf{p}))}{\partial \phi_{og}(\mathbf{r}; \mathbf{p})} \frac{\partial \phi_{og}(\mathbf{r})}{\partial p_j}$$

The first term on the right side in (C.2) is simply the difference between the contrast coefficients. The second term is the derivative of the Heaviside function. In this work, for a c -level set, the Heaviside function is defined as,

$$(C.3) \quad H_\epsilon(x) = \frac{1}{2} \left[1 + \frac{2}{\pi} \tan^{-1} \left(\frac{\pi(x - c)}{\epsilon} \right) \right]$$

The derivative of the Heaviside function is given as,

$$(C.4) \quad \frac{\partial H_\epsilon(\phi_{og}(\mathbf{r}; \mathbf{p}))}{\partial \phi_{og}(\mathbf{r}; \mathbf{p})} = \frac{1}{\epsilon} \left[\frac{1}{1 + \left(\frac{\pi x}{\epsilon} \right)^2} \right]$$

The third term is the derivative of the PaLS function with respect to model parameters. For the old PaLS, we need the derivative of ϕ_{og} in 2.6. The derivatives with respect to different parameters are listed as,

$$(C.5) \quad \frac{\partial \phi_{og}(\mathbf{r}; \mathbf{p})}{\partial \alpha_i} = \psi(\|\beta_i(\mathbf{r} - \boldsymbol{\chi}_i)\|)$$

$$(C.6) \quad \frac{\partial \phi_{og}(\mathbf{r}; \mathbf{p})}{\partial \beta_i} = \alpha_i \frac{\partial \psi(\|\beta_i(\mathbf{r} - \boldsymbol{\chi}_i)\|)}{\partial \beta_i}$$

$$(C.7) \quad \frac{\partial \phi_{og}(\mathbf{r}; \mathbf{p})}{\partial \chi_i^j} = \alpha_i \frac{\partial \psi(\|\beta_i(\mathbf{r} - \boldsymbol{\chi}_i)\|)}{\partial \chi_i^j}$$

where χ_i^j is the j th element of center location of i th basis function $\boldsymbol{\chi}_i$. In this paper, we used basis functions, defined in (3.4), as basis functions to form ψ . Hence the derivative of ψ with respect to β_i , χ_i^j are defined as,

$$(C.8) \quad \frac{\partial \psi(\|\beta_i(\mathbf{r} - \boldsymbol{\chi}_i)\|)}{\partial \beta_i} = -2\beta_i(\mathbf{r} - \boldsymbol{\chi}_i)^T(\mathbf{r} - \boldsymbol{\chi}_i)\psi(\|\beta_i(\mathbf{r} - \boldsymbol{\chi}_i)\|)$$

$$(C.9) \quad \frac{\partial \psi(\|\beta_i(\mathbf{r} - \boldsymbol{\chi}_i)\|)}{\partial \chi_i^j} = 2\beta_i^2(r^j - \chi_i^j)\psi(\|\beta_i(\mathbf{r} - \boldsymbol{\chi}_i)\|)$$

C.1. Derivatives of the 2D PaLEnTIR with respect to model parameters. The PaLEnTIR model can be written as

$$(C.10) \quad f(\mathbf{r}; \mathbf{p}) = C_H(\mathbf{r})T_w(\phi(\mathbf{r}; \mathbf{p})) + C_L(\mathbf{r})(1 - T_w(\phi(\mathbf{r}; \mathbf{p})))$$

The derivative of $f(\mathbf{r}; \mathbf{p})$ with respect to a parameter p_i is written by using the chain rule as,

$$(C.11) \quad \frac{\partial f(\mathbf{r}; \mathbf{p})}{\partial p_j} = (C_H(\mathbf{r}) - C_L(\mathbf{r})) \frac{\partial T_w(\phi(\mathbf{r}; \mathbf{p}))}{\partial \phi(\mathbf{r}; \mathbf{p})} \frac{\partial \phi(\mathbf{r})}{\partial p_j}$$

The transition function has the same definition as of the approximate Heaviside function except we replace ϵ with w . The same holds for the derivative of the transition function.

Similar to the old PaLS model, the third term is the derivative of the PaLEnTIR function with respect to model parameters. We need the derivative of ϕ in 3.2. The derivatives with respect to different parameters are listed as,

$$(C.12) \quad \frac{\partial \phi(\mathbf{r}; \mathbf{p})}{\partial \alpha_i} = \frac{\partial \sigma_h(\alpha_i)}{\partial \alpha_i} \psi(\mathbf{R}_j(\mathbf{r} - \boldsymbol{\chi}_j))$$

$$(C.13) \quad \frac{\partial \phi(\mathbf{r}; \mathbf{p})}{\partial \beta_i} = \sigma_h(\alpha_i) \frac{\partial \psi(\mathbf{R}_j(\mathbf{r} - \boldsymbol{\chi}_j))}{\partial \beta_i}$$

The derivatives with respect to parameters required in equations above are defined as,

$$(C.14) \quad \frac{\partial \sigma_h(x)}{\partial x} = \frac{1}{2} \text{sech}^2\left(\frac{x}{2}\right)$$

$$(C.15) \quad \frac{\partial \psi(\mathbf{R}_j(\mathbf{r} - \boldsymbol{\chi}_j))}{\partial \beta_i} = (-2\mu^2)(\mathbf{r} - \boldsymbol{\chi}_j)^T \begin{bmatrix} e^{2\beta} & 0 \\ \gamma e^\beta & -e^{-\beta} \end{bmatrix} (\mathbf{r} - \boldsymbol{\chi}_j)$$